2019

EFFECT OF HYDROGEN EXPOSURE ON THE ELECTRONIC AND OPTICAL PROPERTIES OF INSULATING TITANATES

John G. Connell
University of Kentucky, johnconnell@uky.edu
Digital Object Identifier: https://doi.org/10.13023/etd.2019.197

STUDENT AGREEMENT:

I represent that my thesis or dissertation and abstract are my original work. Proper attribution has been given to all outside sources. I understand that I am solely responsible for obtaining any needed copyright permissions. I have obtained needed written permission statement(s) from the owner(s) of each third-party copyrighted matter to be included in my work, allowing electronic distribution (if such use is not permitted by the fair use doctrine) which will be submitted to UKnowledge as Additional File.

I hereby grant to The University of Kentucky and its agents the irrevocable, non-exclusive, and royalty-free license to archive and make accessible my work in whole or in part in all forms of media, now or hereafter known. I agree that the document mentioned above may be made available immediately for worldwide access unless an embargo applies.

I retain all other ownership rights to the copyright of my work. I also retain the right to use in future works (such as articles or books) all or part of my work. I understand that I am free to register the copyright to my work.

REVIEW, APPROVAL AND ACCEPTANCE

The document mentioned above has been reviewed and accepted by the student's advisor, on behalf of the advisory committee, and by the Director of Graduate Studies (DGS), on behalf of the program; we verify that this is the final, approved version of the student's thesis including all changes required by the advisory committee. The undersigned agree to abide by the statements above.

John G. Connell, Student

Dr. Ambrose Seo, Major Professor

Dr. Christopher Crawford, Director of Graduate Studies

EFFECT OF HYDROGEN EXPOSURE ON THE ELECTRONIC AND OPTICAL PROPERTIES OF INSULATING TITANATES

DISSERTATION

A dissertation submitted in partial fulfillment of the
requirements for the degree of Doctor of Philosophy in the
College of Arts and Sciences
at the University of Kentucky

By

John Gerard Connell

Lexington, Kentucky

Director: Dr. Ambrose Seo, Associate Professor of Physics

Lexington, Kentucky

2019

ABSTRACT OF DISSERTATION

EFFECT OF HYDROGEN EXPOSURE ON THE ELECTRONIC AND OPTICAL PROPERTIES OF INSULATING TITANATES

Hydrogen exposure of insulating d^0-titanates, such as $SrTiO_3$ (STO), has displayed the formation of intriguing conducting states. These conducting states form through the use of forming gas (N_2/H_2) annealing or hydrogen plasma exposure, where hydrogen gas is exposed to high energy microwaves. The exposure of STO to hydrogen causes metallic conductivity due to the introduction of hydrogen cations on some of the oxygen sites. However, the optical properties of this hydrogen-exposed STO have not been well-studied. Further, $Ba_{0.5}Sr_{0.5}TiO_3$ (BST), an insulating dielectric, also shows changes in its conductivity upon hydrogen exposure. Unlike STO where the conductivity of the hydrogen-exposed material has been characterized, the optical, electronic, and transport properties of hydrogen exposed BST have not been studied. Thus, by studying hydrogen-exposed BST and STO, our understanding of the effects of hydrogen on insulators can be enhanced.

In the first study, the effects of the exposure of insulating dielectric BST thin films to a hydrogen plasma is presented. These BST thin films are deposited on $GdScO_3$ (GSO) substrates via Pulsed Laser Deposition (PLD). After deposition, the thin films are exposed to a hydrogen plasma. Just five minutes of hydrogen plasma exposure is enough to induce conductivity in the BST thin film. This conducting state is dominated by the interplay of disorder and strong electron correlations introduced during hydrogen exposure. Further, the optical properties indicate the formation of a transparent conductor, as the introduction of disorder and strong correlations has not changed the optical properties of the BST thin film in the visible spectrum. BST demonstrates an example of a new type of transparent conductor that utilizes large effective mass carriers to generate conductivity.

In the second study, the effects of hydrogen doping on the surface of STO is explored. The conducting heterointerface that forms between PLD-deposited thin films of $LaAlO_3$ (LAO) on STO is used as the standard to explore this hydrogen surface doping. The optical, electronic, and transport properties of water-leached and buffered hydrofluoric acid (BHF) etched heterointerfaces are characterized and compared. The recently developed water-leaching method is compared with the well-known BHF etching method, which has been shown to unintentionally dope the STO surface with fluorine and hydrogen. Both methods generate single-terminated atomically flat STO

substrate surfaces that are ideal for heterointerface formation. After deposition, the optical, electronic, and transport properties of both the water-leached and BHF-etched heterointerfaces show no meaningful difference, demonstrating that water-leaching may also unintentionally dope the STO substrate surface with hydrogen. However, these results confirm that water-leaching generates a high-quality conducting heterointerface without the safety concerns of BHF.

KEYWORDS: Thin film titanates, pulsed laser deposition, plasma hydrogenation, transparent conductor, conducting heterointerface

John Gerard Connell

(Name of Student)

04/26/2019

Date

EFFECT OF HYDROGEN EXPOSURE ON THE ELECTRONIC AND OPTICAL PROPERTIES OF INSULATING TITANATES

By
John Gerard Connell

Ambrose Seo
Director of Dissertation

Christopher Crawford
Director of Graduate Studies

04/26/2019
Date

To my parents, John and Bernadine, who have been with me on my journey from the beginning.

ACKNOWLEDGMENTS

I would like to express my gratitude to my research advisor Prof. Ambrose Seo for his continuous patience and support during my Ph. D. research here at the University of Kentucky. I am grateful for the time I have had working with him on my projects and learning how to be an effective scientist and researcher.

I would like to thank the members of my committee: Prof. Joseph Brill, whose advice and research collaboration during my time here has been indispensable, Prof. Kwok-Wai Ng, for his insightful comments and encouragement, Prof. John Selegue, for his insightful questions, and my outside examiner, Prof. Marcelo Guzman, for his questions and comments as I completed my dissertation.

I thank my fellow lab members who took this journey with me: Dr. Maryam Souri, Dr. John Gruenewald, Dr. Justin Thompson, Prof. John Nichols, Dr. Oleksandr Korneta, Eric Teipel, Sujan Shrestha, and Jiwoong Kim. I am thankful for their questions, insight, and encouragement throughout my journey. I am also thankful for Namal Wanniniakaye for his advice and hydrogen plasma exposure of the samples discussed in this dissertation. I thank our lab's undergraduate students Brandon Isaac and Mathew Coile and high school student Ronit Kar. There excitement for conducting research kept me going when my projects seemed as if they would never finish.

Finally, I would like to thank my parents, John and Bernadine, who have encouraged me on my journey from the beginning. I also thank my fiancé, Fariba, for her patience and support during my graduate career.

TABLE OF CONTENTS

LIST OF TABLES

LIST OF FIGURES

CHAPTER 1. INTRODUCTION

1.1 Perovskite oxides

Perovskite oxides have attracted substantial attention due to their unique electronic and magnetic properties[1]. These materials have been shown to host strongly-correlated transparent conducting states[2], interfacial conductivity[3-6], interfacial superconductivity[7], interfacial ferromagnetism[8,9], as well as electronic, magnetic, and orbital reconstructions that have led to novel conducting states[10-17]. The key for many of these interesting properties lies in the perovskite structure (ABO_3, where B is typically a transition metal) as shown in Fig. 1.1a.

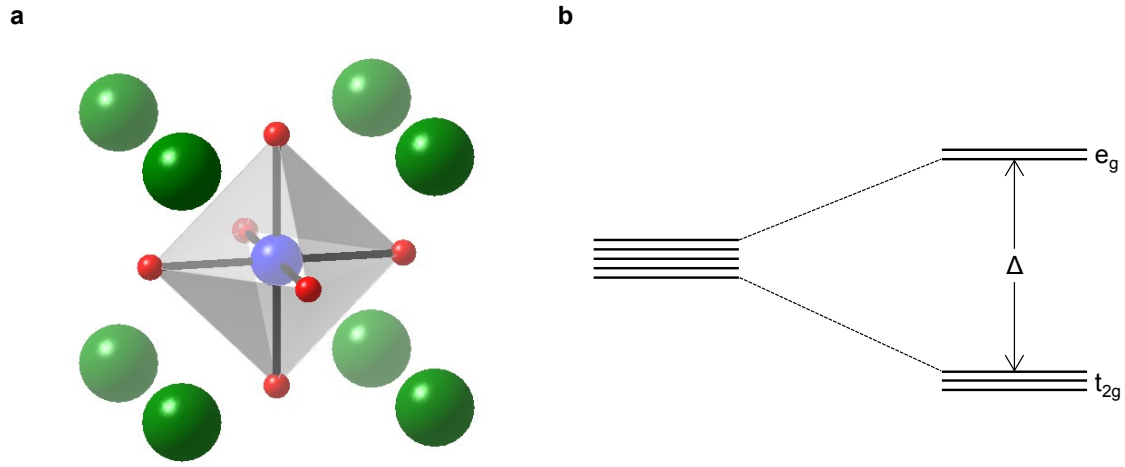

Figure 1.1 Typical perovskite ABO_3 structure and the crystal field splitting due to it. a, typical cubic perovskite unit cell. The A site atoms (green) sit on the corners. The B site (blue) transition metal sits at the center of the unit cell in an octahedron formed by the face-centered oxygens (red). The crystal field splitting of the *d* orbitals is shown in b.

A typical perovskite has an A site atom (typically an alkaline earth or a rare earth metal) that sits on the corners of the unit cell. The B-site transition metal sits in the center of the unit cell, with the oxygen atoms positioned in the face centers. Thus, the B-site atom is

in an octahedral coordination with the surrounding oxygen atoms. This coordination leads to the crystal field splitting of the 5-fold degenerate *d*-orbitals into the 3-fold degenerate t_{2g} and 2-fold degenerate e_g orbitals, as shown in Fig. 1.1b[1]. As we further take correlation effects due to the on-site Coulomb interaction into account, we are able to observe three adjustable degrees of freedom: charge, spin, and orbital[18]. By tuning the structural properties through the introduction of lattice strain, chemical doping, or the use of the broken symmetry at an interface, these degrees of freedom can be tuned to unlock novel physical properties[18]. Chemical doping can be accomplished via chemical substitution (either A site or B site) or the introduction of oxygen vacancies[1,19-22]. Thus, many unique properties and states are available for exploration, which adds to the potential applicability of these materials in current and future devices[18].

In our current investigation, we will focus on the properties of d^0-titanates. Particularly, we will consider a novel doping method on a high dielectric constant d^0-insulator ($Ba_{(1-x)}Sr_xTiO_3$)[23] and the effects of surface preparation on the conducting heterointerface between a d^0-titanate ($SrTiO_3$ (STO)) and a band insulator ($LaAlO_3$ (LAO))[24].

1.1.1 d^0-titanates

d^0-titanates are perovskite oxides where the B-site transition metal is titanium (Ti) and the A-site atom is an alkaline earth metal (typically Ca, Sr, or Ba). These materials can take a cubic (e.g. STO) or tetragonal (e.g. $BaTiO_3$) crystal structure at room temperature. In a simple ionic picture, the *d*-orbital is empty and forms the conduction band above a fully-occupied O_{2p} orbital valence band[1]. Thus, Ti simply becomes a Ti^{4+} cation, while the alkaline earth metal is a cation with a charge of 2+. Depending on the

size of the A-site cation, these systems can show lattice distortions along one of the crystalline axes. These distortions can cause the titanium B-site cation to shift from the center of the perovskite structure, generating a net polarization of the crystal. This polarization can be harnessed via the application of an external electric field, displaying itself as a ferroelectric moment, where an increased static dielectric constant can be observed[1,25].

A large static dielectric constant is not just limited to the tetragonal titanates however. In general, d^0-titanates tend to have a very high static dielectric constant[1]. Figure 1.2 displays the effects of a large dielectric constant on the transport properties of hydrogen plasma reduced STO.

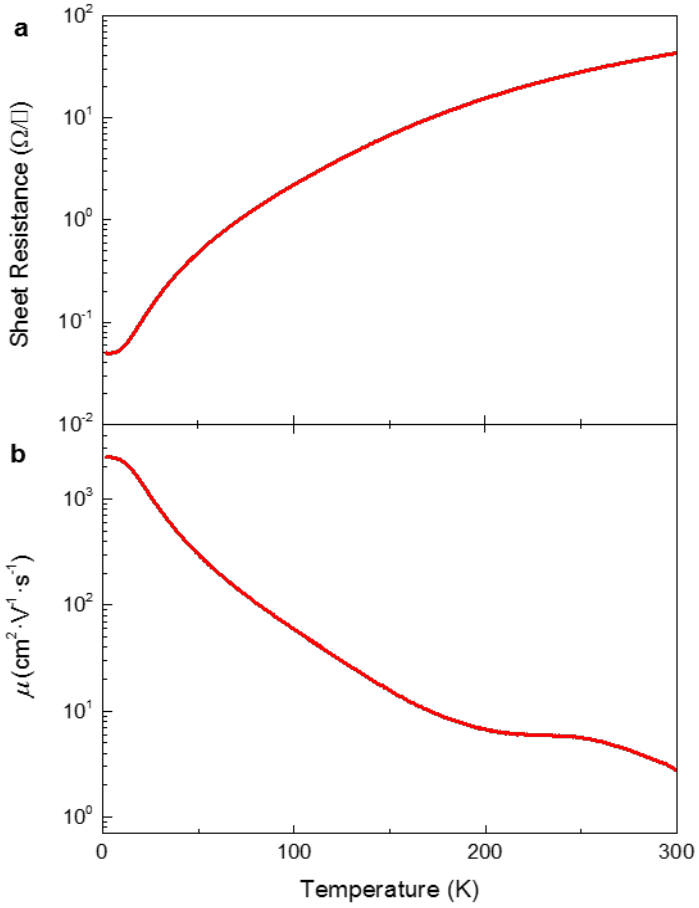

Figure 1.2 Sheet resistance and mobility for a 5 minute plasma hydrogenated (001)-oriented $SrTiO_3$ substrate. The sample displays metallic conductivity at low temperatures in a and an increasing mobility as temperature decreases in b.

At low temperatures, the carrier mobility increases by about 2 orders of magnitude (See Fig. 1.2b), which follows the STO static dielectric constant as it changes from ~300 at 300 K to ~18000 around 2 K[26]. This reduced sample also displays metallic conductivity as shown in Fig. 1.2a. The large dielectric constant in STO follows from the easy accommodation of oxygen vacancies through the generation of shear planes in response

to the addition of these vacancies. These large dielectric constants come from the fact that these perovskite titanates are all close to a structural transition from a cubic to a tetragonal phase, which occurs for BTO at a finite temperature and for STO at 0 K[1]. This increase of the dielectric constant can be observed optically by the softening of the transverse optical phonon mode. As the phase transition is approached, the frequency of this mode tends to zero and the dielectric constant of the material is greatly increased, screening impurities as shown schematically in Fig. 1.3[1,25,27].

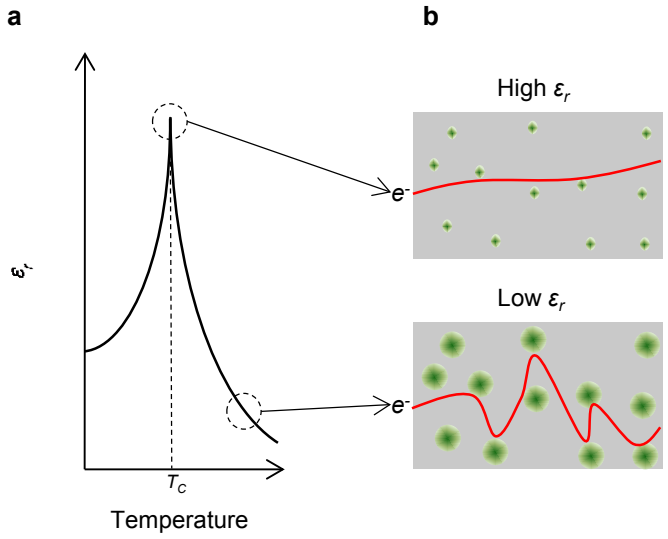

Figure 1.3 How an increasing static dielectric constant can increase carrier mobility. a shows the static dielectric constant (ε_r) versus temperature. T_C indicates the ferroelectric transition temperature. b illustrates the screening of impurities (green dots) as ε_r increases. At low ε_r, electrons are scattered by charged impurities (lower panel, red curve). At high ε_r, charged impurities are more screened and electrons are scattered less, leading to a high carrier mobility near the ferroelectric phase transition.

This increase in the dielectric constant can also be observed by the increase of carrier mobility in Fig. 1.2b. As the phase transition is approached the increased dielectric constant screens impurities and the conducting electrons are less scattered, which

increases the mobility as shown schematically in Fig. 1.3b[1,28]. Thus, carrier doping of high dielectric constant d^0-titanates can lead to unique high mobility conducting states.

1.1.2 Effects of electron doping on d^0-titanates

As a d^0-titanate is electron doped, the system can undergo an insulator to metal transition, as illustrated in Fig. 1.4.

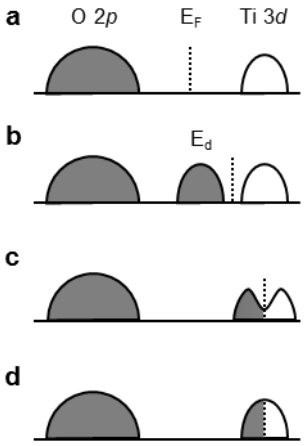

Figure 1.4 Schematic representation of doping a d^0-titanate. a, typical insulating d^0-titanate before carrier doping. Note that the filled valence band is O 2*p* in character and the unfilled conduction band is Ti 3*d* in character[1]. b, after adding impurities, an impurity state (E_D) forms, raising the Fermi level (E_F). c, as more impurities are added, scattering of charged impurities leads to Anderson localization and the conductivity is not metallic. d, at a high enough doping level, electrons enter the conduction band and metallic conductivity occurs.

First, as impurities are added to the system, an impurity band (E_D) forms between the filled valence band (VB, O 2*p* for a d^0-titanate) and the unfilled conduction band (CB, Ti 3*d*), shifting the Fermi energy (E_F) of the system to sit between this filled impurity band and the unfilled conduction band (See Fig. 1.4b). Then, as even more impurities are added to the system, the impurity band begins to overlap with the conduction band, as shown in Fig. 1.4c. However, strong disorder in a doped compound leads to Anderson

localization; the conducting electrons interact with charged impurity sites, which limits the overall conductivity of the system[22,29-31]. Finally, at a high enough doping level, the impurity band broadens and electrons enter the conduction band of the material, completing the transition to the metallic state, as shown in Fig. 1.4d[1]. Note that Fig. 1.4 ignores the effects of strong electron correlations. The implications of these effects on the insulator-to-metal transition will be discussed in Chapter 2.

An interesting question can be raised at this point. Namely, is conductivity easily generated via doping in all d^0-titanate materials? If we consider only the single-occupied A-site compounds $SrTiO_3$ and $BaTiO_3$, the answer appears to be yes[1,19-22,32-37]. Both materials are quite susceptible to chemical doping and oxygen vacancy-based conductivity. However, despite the high room temperature dielectric constant in BTO ($\sim 10^3$)[38], there has been no report of an enhanced mobility[33-37]. Regardless, we would expect the mixed A-site perovskite $Ba_{(1-x)}Sr_xTiO_3$ to similarly form a conducting or semiconducting state using conventional doping techniques such as the addition of oxygen vacancies or cation doping. It would be advantageous to generate conducting $Ba_{(1-x)}Sr_xTiO_3$ as the dielectric constant tends to be about an order of magnitude higher ($\sim 10^4$) than BTO at room temperature[38,39]. However, no measurable dc conductivity is introduced via conventional means of doping[23,40]. Thus, we can ask, are there any doping methods that can cause metallic conductivity in $Ba_{(1-x)}Sr_xTiO_3$?

1.2 Exposure of insulating oxides to hydrogen

Hydrogen exposure of d^0-titanates is another method of generating semiconducting and conducting states[1,19,20,41-45]. Here, oxide materials are typically exposed to forming

gas (N_2/H_2 or Ar/H_2) at high temperatures[46,47], vacuum sealed with a metal hydride (e.g. CaH_2) and heated[42-45], exposed to H^+ cations via ionic liquid gating[48-50], or exposed to a hydrogen plasma[51,52]. Two of these methods have been employed on $Ba_{(1-x)}Sr_xTiO_3$, leading to intriguing results as discussed in Subsections 1.2.1 and 1.2.2[51,53-57].

Following the discussion of $Ba_{(1-x)}Sr_xTiO_3$, we consider a second question. Namely, can unintentional surface hydrogen doping influence the surface and interfacial properties of a single crystal substrate[24]? The mechanisms of this unintentional surface doping will be discussed in Subsection 1.2.3.

1.2.1 Forming gas annealing of insulating oxides

Forming gas annealing is typically used in the semiconductor industry to eliminate the interfacial traps present in the Si-SiO_2 system[58,59]. The typical processing temperature for forming gas annealing is around 400 °C with an anneal lasting a few hours[46,57-59]. The effects of forming gas on oxides has been investigated for some time[19,20,41]. Recently, the performance of $Ba_{(1-x)}Sr_xTiO_3$ capacitors after forming gas exposure has been investigated[53-55]. These materials have been considered as a new *high-k* dielectric for use in the semiconductor industry[39,60-62]. Thus, it is important to determine whether $Ba_{(1-x)}Sr_xTiO_3$ capacitors can withstand a forming gas anneal. However, it has been shown that forming gas decreases the static dielectric constant of $Ba_{(1-x)}Sr_xTiO_3$ and increases the observed leakage current in all reported cases[53-56]. Further, oxygen annealing following forming gas annealing does not restore the degraded capacitor back to its original performance, although there is some improvement[54,56]. However, an investigation of the structural, transport, and optical properties after hydrogen exposure has not been conducted. Thus, a thorough study of the properties of

these hydrogen exposed $Ba_{(1-x)}Sr_xTiO_3$ systems is a must to understand the unique effects of hydrogen, as these effects appear to be different from what is observed in STO and BTO[19,20,41,42]. However, forming gas annealing is a process that takes a few hours. After a few hours of exposure, most oxides turn completely black, which can make it difficult to fully understand the optical properties[46]. Thus, we seek a short-term hydrogen exposure process to explore the effects in $Ba_{(1-x)}Sr_xTiO_3$.

1.2.2 Hydrogen plasma exposure of insulating oxides

Hydrogen plasma exposure provides a short-term method of hydrogen exposure. A microwave plasma chamber is shown with a schematic of its operation in Fig. 1.5.

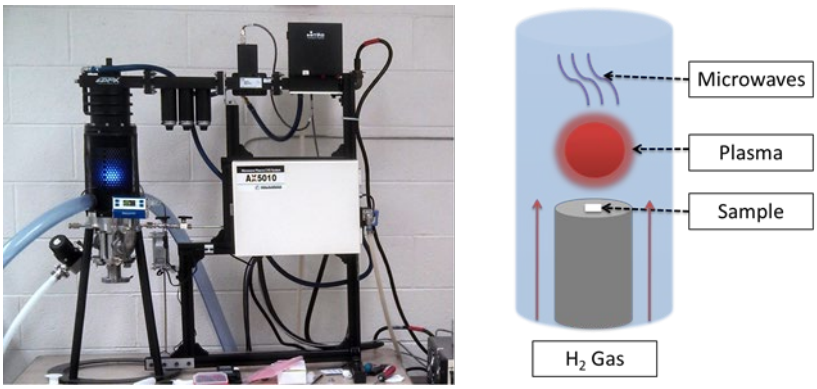

Figure 1.5 Plasma hydrogenation chamber (left) with a schematic of how materials are hydrogenated (right).

As shown in the schematic, the process gas enters from the bottom of the chamber while high energy microwaves are generated from the top of the chamber. The interaction between the microwaves and H_2 causes a plasma containing H_2, H^+, and free electrons to form. Finally, a sample can be removed from the hydrogen plasma chamber within a few minutes to an hour of processing, as opposed to cool-down time of about 12 hours after forming gas annealing. All plasma hydrogenation experiments in this work have been

conducted by Allen D. Reed (STO single crystal) and Namal Wanninayake ($Ba_{0.5}Sr_{0.5}TiO_3$ thin film) in Prof. Doo Young Kim's laboratory in the Chemistry Department at the University of Kentucky. Further discussion of the plasma hydrogenation conditions used for the $SrTiO_3$ single crystal and $Ba_{0.5}Sr_{0.5}TiO_3$ thin films can be found in the Methods section of Chapter 2.

Previous short-term hydrogen plasma exposure shows similar results in $Ba_{(1-x)}Sr_xTiO_3$ as compared with forming gas annealing. Morito *et al*. has shown that 10 minutes of exposure to a CH_4 plasma can have similar effects on the leakage current of $Ba_{(1-x)}Sr_xTiO_3$ capacitors as compared with forming gas annealed samples[51]. Short-term exposure of $Ba_{(1-x)}Sr_xTiO_3$ can allow for an investigation of the optical properties. For example, just 5 minutes of hydrogen plasma exposure generates a metallic optical response in the transmittance of the single crystal STO substrate in Fig. 1.6, while not drastically reducing the optical transparency in the visible region.

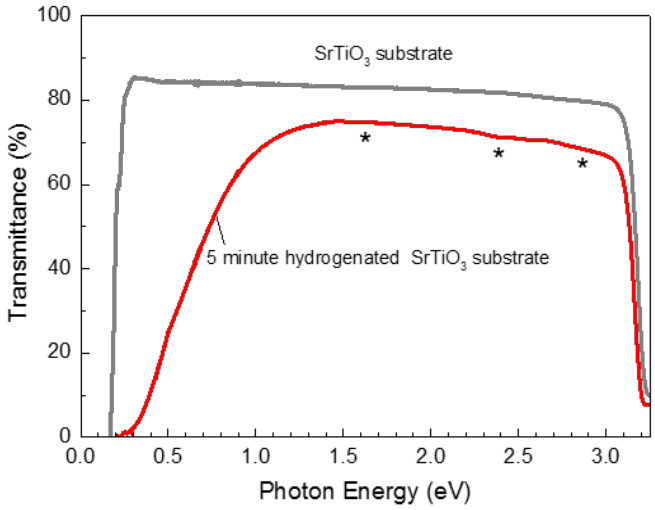

Figure 1.6 Transmittance of a (001)-oriented $SrTiO_3$ substrate before and after 5 minutes of plasma hydrogenation. The hydrogenated substrate shows a metallic Drude response, which agrees with the metallic conductivity measured in Fig. 1.2a. The asterisks (*) at 1.7, 2.4 and 2.9 eV indicate the optical absorptions due to oxygen vacancies[19,20].

These optical properties can be well-explained by an oxygen vacancy interpreteation[19,20]. However, for $Ba_{(1-x)}Sr_xTiO_3$, this explanation may not be completely valid since the insulating properties of $Ba_{(1-x)}Sr_xTiO_3$ capacitors are not fully restored upon oxygen annealing[51,54]. Thus, a study of the effects of hydrogen plasma exposure on the optical and conducting properties of $Ba_{(1-x)}Sr_xTiO_3$ can shed light on the conducting mechanism present in a high dielectric constant insulator. The results of this study are presented in Chapter 2.

1.2.3 Unintentional surface hydrogen doping of insulating oxides

Through the use of wet surface preparation methods, the crystal surface of oxides can be unintentionally doped with hydrogen. This surface hydrogen has been observed in

(001)-oriented $SrTiO_3$ substrate surfaces via the most common preparation method: buffered hydrofluoric acid etching (BHF-etching)[63]. This method is intended to generate an atomically flat TiO_2-terminated surface. The formation of this surface is necessary to generate the 2 dimensional electron gas (2DEG) present at the heterointerface of $LaAlO_3$ and $SrTiO_3$ and generate a high quality single-terminated substrate surface[3,63]. However, BHF-etching has been shown to unintentionally dope the STO substrate surface with hydrogen and fluorine, potentially changing the interfacial electronic properties[64-66]. Hatch *et al*. has shown that the unintentional fluorine doping generates a deep trap state, while unintentional hydrogen doping generates a shallow state that may contribute to the interfacial electronic properties[64]. Further, Hatch *et al*. goes on to show that by using boiling water to prepare the surface, only some oxygen vacancies form[64]. Hence, they go on to claim that the best single-terminated STO surface is generated by exposure to boiling water[67]. However, a room temperature Deionized-water leaching (water-leaching) method has been shown to also generate a single-terminated atomically flat STO substrate surface[68]. Thus, a comparison between the BHF-etching method and the water leaching method using the conducting heterointerface between $LaAlO_3$ and $SrTiO_3$ may shed light on the effects of surface hydrogen and fluorine doping[24]. The results of this study are presented in Chapter 3.

1.3 d^0-titanate thin films and heterointerfaces

In order to investigate the fundamental effects of hydrogen plasma exposure and unintentional surface hydrogen doping, we will consider thin films and thin film heterointerfaces, respectively. In the case of hydrogen plasma exposure, considering a thin $Ba_{(1-x)}Sr_xTiO_3$ film will allow us to fully quantify the optical and transport properties

of this system. Further, thin films are often incorporated in many current commercially available devices, allowing for the discussion of potential applications of these materials[18,69]. Thus, we will consider two thin film systems to investigate the questions that have been indicated above: $Ba_{0.5}Sr_{0.5}TiO_3$ deposited on single-terminated atomically flat $GdScO_3$ substrates[70] and $LaAlO_3$ deposited on single-terminated $SrTiO_3$ substrates[63,68].

1.3.1 Titanate thin films: $Ba_{0.5}Sr_{0.5}TiO_3$

Thin films of $Ba_{0.5}Sr_{0.5}TiO_3$ (BST) are deposited via pulsed laser deposition (PLD) on (110)-oriented $GdScO_3$ substrates in the PLD chamber shown in Fig. 1.7.

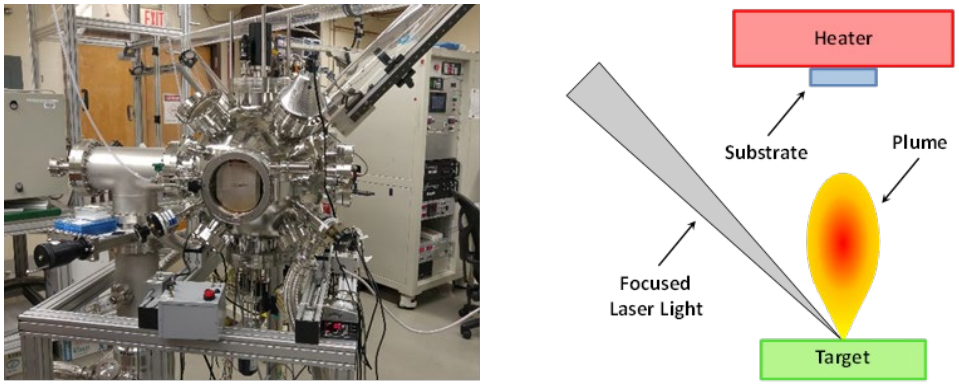

Figure 1.7 Pulsed laser deposition (PLD) vacuum chamber (left) with a schematic of PLD (right). As laser light is focused on a target, a plume of target material is generated that deposits a thin film on the heated substrate.

Thin films have been deposited by using two single crystal $SrTiO_3$ and $BaTiO_3$ targets. The stoichiometry has been controlled by alternating each target every half-unit cell. After deposition, thin films are exposed to a hydrogen plasma using the hydrogen plasma chamber in Fig. 1.5. After exposure, the structural, electronic, and optical properties have been measured and interpreted. The results of this data and its implications on our

understanding of ionic disorder and strong-electron correlations introduced by non-equilibrium hydrogen plasma exposure are discussed in Chapter 2[23].

1.3.2 Heterointerfaces: $LaAlO_3/SrTiO_3$

Conducting heterointerfaces of $LaAlO_3/SrTiO_3$ (LAO/STO) are generated via pulsed laser deposition of a $LaAlO_3$ (LAO) target simultaneously on two $SrTiO_3$ substrates. The STO substrates are cut from the same larger substrate in order to ensure the uniformity of the substrate surface. The only difference between the two substrate halves is the preparation method: one substrate is prepared using BHF-etching[63], while the other is prepared using water leaching[68]. After deposition, the structural, electronic, and optical properties of the heterointerfaces have been measured and interpreted. The results of this data and its implications on our understanding of surface doping of wet etched substrates is discussed in Chapter 3[24].

1.3.3 Thin film deposition via Pulsed Laser Deposition (PLD)

Pulsed Laser Deposition (PLD) is a physical vapor deposition technique utilized to generate high-quality thin films and heterointerfaces. As shown in Fig. 1.7, a vacuum chamber (base pressure: $\sim 10^{-8}$ Torr) is used to allow the laser ablated target material (See the schematic in Fig. 1.7) to be deposited on the substrate. The beam is optically steered and focused from a KrF excimer laser ($\lambda = 248$ nm) and is directed at a stoichiometric single crystal target. The laser plume generated from the interaction of the laser and the target contains the constituents of the target material less some oxygen, which is lost due to the energy of the laser plume. Thus, a background oxygen partial pressure (pO_2) is employed in order to ensure proper thin film stoichiometry, with typical values being between 10^{-6} Torr (oxygen deficient) up to about 250 milliTorr (mTorr). The substrate

upon which the thin film is deposited is maintained at high temperatures, typically around 500-800 °C. The optimal value of the substrate temperature usually corresponds to about half of the melting temperature of the thin film being deposited. A properly heated substrate increases the probability that a high quality epitaxial thin film will form.

After deposition, the thin film is cooled either at the same, higher, or lower pO_2 as has been used during deposition. This value is adjusted to influence the oxygen content of the thin films. By cooling at a low pO_2, oxygen vacancies will be incorporated in the thin film, which will most likely cause metallic or semi-metallic conductivity. By cooling at the same or higher pO_2, these oxygen vacancies can be limited so that the deposited thin film will be insulating. The thin films deposited and discussed in the following chapters have both been deposited at 700 °C with deposition pressures ranging from 10^{-6} Torr to 10 mTorr and cool-down pressures ranging from 10 mTorr to 1 Torr. A detailed discussion on the design and operation of the vacuum chamber displayed in Fig. 1.7 is located in Appendix A.2.

CHAPTER 2. TRANSPARENT CONDUCTING STATES INDUCED BY HYDROGEN-PLASMA

Transparent conducting oxides (TCO) are essential materials for advanced optoelectronic devices such as display panels and solar cells. One example is tin doped indium oxide, i.e. Sn: In_2O_3, the most commonly-used TCO, which shows high electronic conductivity with optical transparency. However, doping with heavy ions such as tin has been a fundamental barrier in enhancing the properties of TCO's due to strong impurity scattering. Here, we report a new method for generating TCO's: applying the lightest element (hydrogen) to insulating dielectric oxides. By exposing $Ba_{0.5}Sr_{0.5}TiO_3$ (BST) thin films to hydrogen plasma for a few minutes, we have formed an optically-transparent, electrically-conducting state. We have found that this transparent conducting state is induced by the confluence of strong electron-correlation and ionic disorder. The discovery of this new transparent conducting state opens new opportunities not only for device applications but also for understanding the behavior of strongly-correlated electrons in non-equilibrium states.

2.1 Introduction

Transparent conducting oxides (TCO's) are indispensable materials for modern optoelectronic components, such as display panels and solar cells[69,71]. TCO's should exhibit high electronic conductivity ($\sigma > 10^4$ S/m) with good optical transparency (> 80 %) in the visible photon energy region (1.6 – 3.0 eV)[72]. The most widely-used TCO's, e.g. Sn: In_2O_3 and $(In, Ga)_2ZnO_7$, satisfy this property[72,73]. However, heavy ion doping in typical TCO materials introduces strong impurity scattering, limiting their electronic conductivities[73]. Moreover, the ever increasing cost of indium has driven the search for

new methods of creating transparent conducting materials. Unfortunately, this effort has proven to be a formidable task because most undoped oxides are good insulators, whose conducting phases require at least a few percent of heavy ion doping. This amount of doping generates a huge amount of impurities compared to conventional ppm doping in semiconductors, which introduces inevitable optical absorption bands in the visible spectrum[19,20]. Recently, metallic oxides such as $SrVO_3$ (SVO) have been proposed to create transparent conducting states due to the large effective mass of strongly-correlated electrons that can lower the plasma frequency below 1.6 eV for optical transparency[2]. Hence, it would be ideal to find a way to utilize the benefits of the large effective mass of strongly correlated electrons with minimal impurity scattering in the continued search for new TCO's.

In this chapter, we report the first observation of unprecedented transparent conducting states generated in a dielectric oxide thin film by doping hydrogen, the lightest element, in a thermodynamically non-equilibrium manner. Through the utilization of hydrogen plasma exposure, insulating $Ba_{0.5}Sr_{0.5}TiO_3$ (BST) thin films maintain good transparency in the visible region while becoming conducting. Our approach of short-term (i.e. for a few minutes) hydrogen plasma exposure differs from conventional plasma hydrogenation, forming gas annealing, metal hydride reduction, and ionic liquid gating where samples are typically exposed for a few hours[42,44,45,47-51,53-57]. While long-term hydrogen exposure can reduce optical transparency, short-term hydrogen plasma exposure preserves good optical transparency as identical to the as-deposited, insulating BST thin films in the visible spectra (See Fig. 2.6b). Moreover, we have discovered that as hydrogen plasma exposure time increases, the BST thin films

undergo a phase transition from a dielectric band insulator, to a disordered insulator, and finally to a transparent conductor. This phase transition is driven by the confluence of strong-electron correlation and ionic disorder induced by the hydrogen plasma exposure. These results demonstrate that short-term hydrogen plasma exposure of insulating dielectrics can generate novel transparent conducting states that will pave the way to develop new optoelectronic materials.

2.2 Methods

We have synthesized epitaxial $Ba_{0.5}Sr_{0.5}TiO_3$ thin films by pulsed laser deposition. $Ba_{0.5}Sr_{0.5}TiO_3$ (BST) thin films are deposited on (110)-oriented $GdScO_3$ substrates, which has an in-plane lattice match of (+0.50 %), using a KrF excimer laser with a laser fluence of 1.6 J/cm^2 at 700 °C with an oxygen partial pressure of 10 mTorr. We have synthesized epitaxial BST thin films on (110)-oriented $GdScO_3$ substrates, using pulsed laser deposition[74]. Thin films are deposited from $BaTiO_3$ and $SrTiO_3$ targets that are switched after each half-unit cell of deposition until a 75 nm thick film is deposited. The thin films are cooled with a 1 Torr oxygen background to ensure proper oxygen stoichiometry. The (110)-oriented $GdScO_3$ substrates are prepared by annealing in air at 1000 °C for one hour, which produces a single-terminated atomically-flat substrate surface as confirmed by atomic force microscopy (Park Systems) (See Fig. 2.12)[70]. The amorphous thin films have been deposited with a thickness of about 20 nm on glass at room temperature (~25 °C) using the same laser conditions and pO_2 used for the crystalline samples. The crystallinity and thickness of the thin films is confirmed by X-ray diffractometry (Bruker D8 Advance) (See Fig. 2.11). BST thin films are plasma hydrogenated from 2-5 minutes (1 hour for amorphous samples) using a microwave plasma CVD system (Seki Diamond

Systems, AX5010, 2.45 GHz), which generates a plasma using 300 W microwaves in a H_2 partial pressure of 10 Torr. Scanning transmission electron microscopy is conducted using an FEI Titan SEM. The optical transmittance and reflectivity of the thin films is measured using a grating type spectrophotometer for energies from 6 eV to 0.5 eV and a Fourier Transform Infrared Spectrometer from 50 meV to 0.6 eV. Resistivity and transport measurements to 2 K are conducted using a physical property measurement system (Quantum Design PPMS) with a maximum magnetic field of 14 T. Chemical states present in the as-deposited BST, hydrogenated BST, and oxygen deficient BST thin films have been examined via X-ray photoelectron spectroscopy (XPS) using a Thermo Scientific K-Alpha photoelectron spectrometer. XPS measurements have been performed by focusing monochromatic Al K-α radiation (energy of 1486.6 eV) onto each sample with a spot diameter of 400 μm.

2.3 Conducting properties of hydrogen plasma exposed BST thin films

Hydrogen plasma exposure introduces carriers to the BST thin films, which become conducting after about 5 minutes of exposure. Figure 2.1a shows the temperature- dependent resistivity of the BST thin films exposed to hydrogen plasma from 2 to 5 minutes.

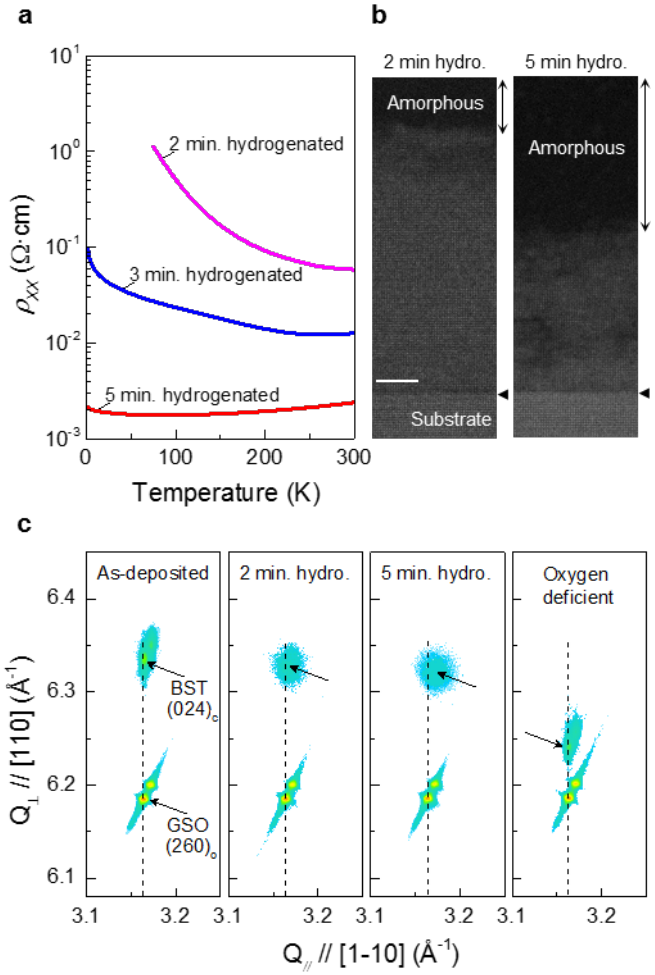

Figure 2.1 The effects of plasma hydrogenation on the electronic and structural properties of BST thin films. a, Resistivity vs. temperature for BST thin films plasma hydrogenated from 2-5 minutes. b, HAADF STEM of the 2 minute and 5 minute hydrogenated thin films. The black arrows indicate the approximate size of the amorphous regions. The white scale bar is 15 nm. c, RSM scans about the GSO 260_O reflection for the as-deposited, hydrogenated, and oxygen deficient thin films. As the resistivity decreases, the size of the amorphous layer increases with longer hydrogen plasma exposure. Both the as-deposited and oxygen deficient thin films show no measurable conductivity.

Samples with a hydrogen plasma exposure time shorter than 2 minutes remained highly insulating, disallowing reliable dc-resistivity measurements. Note that the 2 and 3 minute hydrogenated thin films show some reduced resistivity but exhibit insulating behavior ($d\rho/dT < 0$). As hydrogenation time increases to 5 minutes, the BST thin film displays

correlated metallic behavior[32,75,76]. Coinciding with this decrease in resistivity, the scanning transmission electron microscopy images in Fig. 2.1b reveal the formation of an amorphous-like layer from the surface, which increases in thickness as the exposure time is increased. Further evidence of this amorphous-like layer is shown by the large diffuse spread of the (024) BST thin film peak in the x-ray reciprocal space maps shown in Fig. 2.1c. The formation of similar amorphous-like layers has been previously observed for hydrogenated TiO_2 nanoparticles, which enhances their photocatalytic properties significantly[46,52,77,78]. Similarly, we have found that this amorphous-like layer contributes to the conducting properties of all hydrogenated BST thin films, as discussed in the following Subsection.

2.3.1 Conducting properties of insulating BST

Plasma hydrogenated insulating $Ba_{0.5}Sr_{0.5}TiO_3$ (BST) thin films show differeing behavior at high and low temperatures. The insulator fits for the 2 minute hydrogenated, 3 minute hydrogenated, and amorphous 1 hr. hydrogenated thin films are displayed in Fig. 2.2.

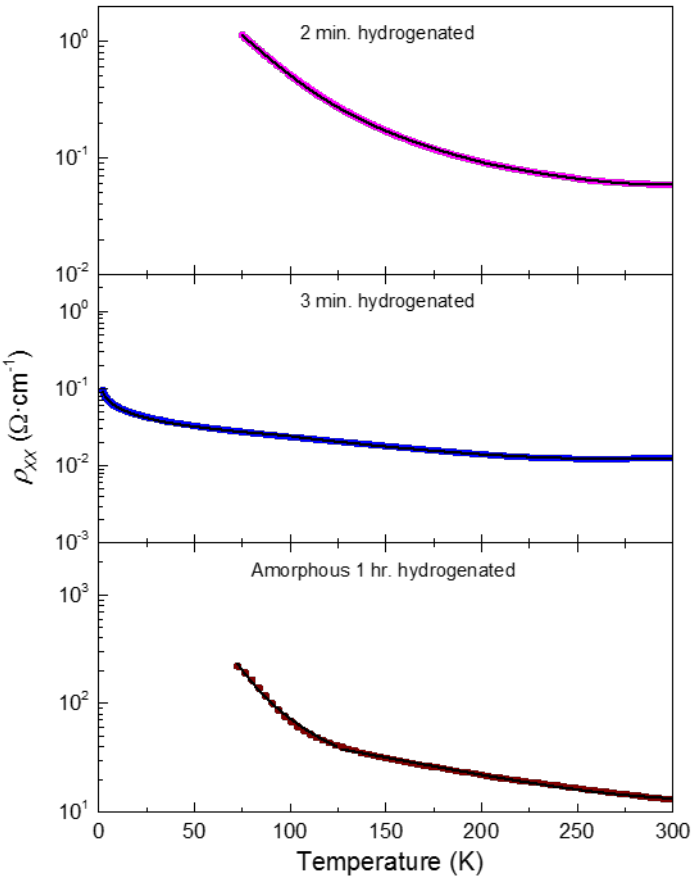

Figure 2.2 Properties of insulating BST thin films. Resistivity vs. temperature for the 2 minute, 3 minute, and amorphous 1 hour hydrogenated BST thin films. The black lines are fits of the resistivity (See Table 1).

All three samples could not be fit using a simple single insulating fit of any form. At high temperatures, all 3 samples can be fit by the following weak localization model,

$$\rho(T) = \rho_0 - \alpha T^{3/4} + \beta T^{3/2} \tag{2.1}$$

where ρ_0, α, and β represent the remnant resistance, weak localization, and electron-boson interaction contributions, respectively[75]. As shown in Table 2.1, as hydrogenation time increases, weak localization can be fit to lower temperatures.

Table 2.1 Resistivity fits for BST hydrogenation times at various temperatures.

Hydrogenation Time	Temperature range (K)	Fitting Function $\rho(T)$ (Ω•cm)[2]
2 minutes	$200 \leq T \leq 300$	$\rho_0 - \alpha T^{3/2} + \beta T^{3/4}$
	$50 \leq T < 200$	$(1/\rho_0 \exp(T_G/T) + 1/\rho_1)^{-1}$
3 minutes	$100 \leq T \leq 300$	$\rho_0 - \alpha T^{3/2} + \beta T^{3/4}$
	$2 \leq T < 100$	$(1/\rho_0 \sqrt{T} \exp((T_M/T)^{1/4}) + 1/\rho_1)^{-1}$
5 minutes	$2 \leq T \leq 300$	$\rho_0 - \alpha T^{3/2} + \beta T^{3/4}$
1 hour[1]	$125 \leq T \leq 300$	$\rho_0 - \alpha T^{3/2} + \beta T^{3/4}$
	$75 \leq T < 125$	$\rho_0 \exp(T_G/T)$

1 Amorphous thin film (20 nm thickness)
2 Fit curves are the black lines in Figure 2.2 and Figure 2.3 (5 minute sample)

After 5 minutes of hydrogen plasma exposure weak localization fits the entire temperature region to 2 K (See Figure 2.4).

The insulating samples show rich behavior at low temperatures. The 2 minute hydrogen plasma exposed and 3 minute hydrogen plasma exposed samples low temperature behavior cannot be fit by a single insulator. In fact the samples are fit by,

$$\rho(T) = \left(\frac{1}{\rho_0 e^{\frac{T_G}{T}}} + \frac{1}{\rho_1}\right)^{-1} \tag{2.2}$$

for the 2 minute sample where $T_G = \frac{E_G}{2k_B}$, and

$$\rho(T) = \left(\frac{1}{\rho_0 \sqrt{T} e^{\frac{T_M}{T}^{1/4}}} + \frac{1}{\rho_1}\right)^{-1} \tag{2.3}$$

for the 3 minute sample where $T_M = \frac{18}{k_B\, N(E_F)\, a^3}$, and $N(E_F)$ and a are the density of states at the Fermi level and the localization length, respectively[32,79,80]. Both samples require the addition of a linear insulator in parallel, which we have dubbed ρ_1 that will be further discussed below. Adding multiple insulator fits in parallel, such as the Arrhenius or Mott models, does not lead to a fit of our data (not shown). Finally, the low temperature behavior of the amorphous hydrogen plasma exposed sample can be fit by a single insulator of the form

$$\rho(T) = \rho_0 e^{\frac{T_G}{T}} \tag{2.4}$$

From the insulator fits, we find that the 2 minute hydrogen plasma exposed sample has a very narrow gap of about 67.6 meV and the 3 minute hydrogen plasma exposed sample displays a T_M value of 0.71 K. This small value indicates that the 3 minute sample is close to the insulator-to-metal transition, which is likely due to a large $N(E_F)$[30,81]. Further, the transition from an "Arrhenius-like" to a "Mott-like" fit indicates that as hydrogenation time increases, the electronic band gap continues to close, as indicated by the optical conductivity in Figure 2.8[32]. It is noteworthy that both fits require the addition of a constant parallel resistor whose resistivity is denoted as ρ_1. The inclusion of this parallel resistivity suggests that both the amorphous-like and crystalline regions contribute to the observed transport properties (See Fig. 2.1b, particularly the 2 minute hydrogen plasma exposed sample and Fig. 2.10).

The amorphous BST thin film requires 1 hour of hydrogen plasma exposure to show a measurable conductivity. The low temperature region displays a narrow gap with a value of 52.9 meV. This gap is narrower than the 2 minute hydrogen plasma exposed

sample, which is most likely due to the long hydrogen plasma exposure time. The reason for the longer time may be related to the fact that the amorphous thin film receives ionic disorder during PLD deposition (See the Methods seciton for depostion conditions), whereas the crystalline thin films receive ionic disorder from hydrogen plasma exposure (See Fig. 2.1 and Fig. 2.10b).

2.3.2 Transport properties of conducting BST

Turning our attention to the 5 minute hydrogen plasma exposed thin film, we can fit the resistivity using a weak localization model for all measured temperatures (See Fig. 2.4), demonstrating that the ionic disorder introduced by hydrogen plasma exposure is a contributing factor to the observed conductivity[46].

The temperature-dependent resistivity of the 5 minute hydrogen plasma exposed BST thin film displays weak localization behavior (See Fig. 2.4), which is a disorder driven effect due to quantum interference of the conducting carriers at defect sites[82]. This method of conductivity suggests that the ionic disorder introduced by hydrogen plasma exposure is a contributing factor to the observed electronic transport (See Fig. 2.1a and 2.1b)[46]. Further measurements under magnetic fields suggest that ionic disorder and the Coulomb interaction between carriers play an important role in the hydrogen plasma exposed BST thin films. To differentiate between weak localization and anti-localization, the magnetoresistance (*MR*) of the 5 minute hydrogenated thin film is measured as shown in Fig. 2.3.

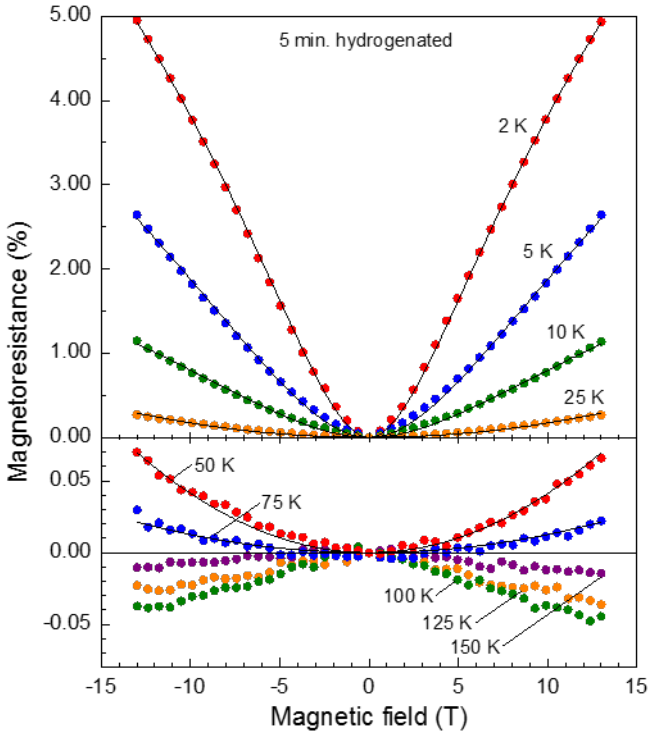

Figure 2.3 Magnetoresistance (*MR*) for the conducting 5 minute plasma hydrogenated BST thin film. The low temperature *MR* from 2 K to 25 K is plotted above the *MR* from 50 K to 150 K. At 2 K, 5 K, and 10 K the *MR* is fit by $MR = (\frac{1}{BH^2} + \frac{1}{CH^{1/2}})^{-1}$, due to strong electron correlations and high-field spin-splitting in the BST thin film. From 25 K to 75 K, the *MR* is fit by $MR = AH^2$ due to strong electron correlations. Above 75 K, the *MR* is negative indicating weak localization in the BST thin film due to disorder. The transition from a negative to positive *MR* is due to the opening of the Coulomb gap due to electron-electron interactions.

From 150 K to 100 K, the *MR* is negative, which is due to the asymmetrical phase shift between forward and backscattered carriers that suppresses the interference, i.e., weak localization, and results in a decrease in the resistance under magnetic fields[82]. From 75 K to 25 K, the magnetoresistance is positive and can be fit by the familiar Lorentz behavior, i.e. $MR = AH^2$, where *A* is a constant. At 10 K and below, the *MR* is given by $MR = (\frac{1}{BH^2} + \frac{1}{CH^{0.5}})^{-1}$, where *B* and *C* are constants. The low temperature behavior is

due to the Coulomb interaction between electrons (H^2) with spin-splitting ($H^{0.5}$) manifesting below 10 K at high fields, as shown in Fig. 2.4.

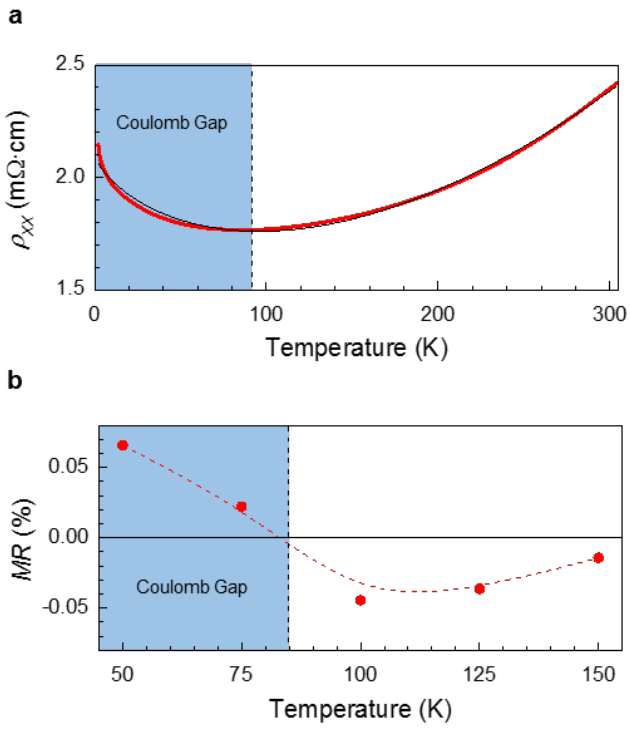

Figure 2.4 Observation of the Coulomb gap in 5 minute hydrogenated BST. a, resistivity vs. temperature for the 5 minute hydrogen plasma exposed BST thin film. The black line is the weak localization fit (See Table 2.1). b, the maximum magnetoresistance (*MR*) vs. temperature. The crossover from a negative to a positive *MR* occurs at the same value as the increase in resistivity shown in a. This crossover indicates the opening of the Coulomb gap. The plotted *MR* values are taken at +14 T.

As shown above around 75 K, a transition from a negative to a positive magnetoresistance (*MR*) is observed (See Fig. 2.4b and Fig. 2.3). This transition corresponds to the transition from metallic to insulating behavior as shown in Fig. 2.4a. Due to the presence of a large number of conducting carriers (See Fig. 2.5a), this gap is likely due to the Coulomb interaction between electrons (Coulomb gap), which has been

observed in heavily-doped semiconductors at low temperatures[31,83,84]. Similar observations have been seen in heavily-doped semiconductors such as Si:P (Ref. [83]).

The appearance of the Coulomb interaction between electrons agrees well with our Hall measurements that give a carrier concentration of $n = 1.67\times10^{22}$ cm^{-3}, which is about one electron per titanium ion (See Fig. 2.5a).

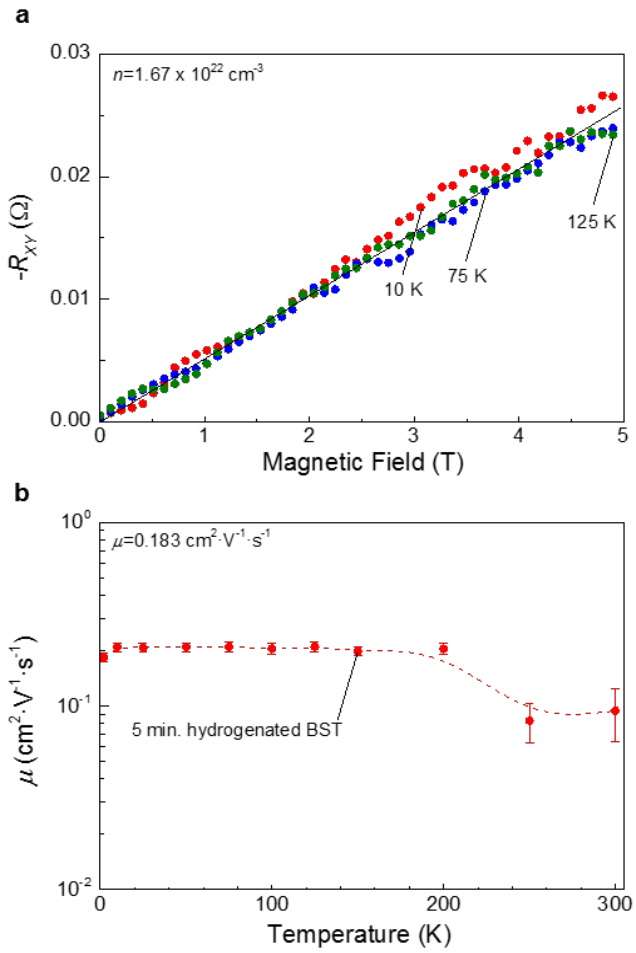

Figure 2.5 Transport properties for 5 minute hydrogenated BST. a, Hall resistance vs. magnetic field (T) for the 5 minute hydrogen plasma exposed BST thin film. The black line is an eye guide demonstrating the similarity of the Hall data across varying temperatures. b, carrier mobility vs. temperature. Note that the mobility is constant with temperature. The dotted red line is an eye guide.

Very little variance in the Hall resistance is observed as the temperature increases. From fitting the slope of our Hall resistance, we extract an average carrier concentration of $n = 1.67 \times 10^{22}$ cm^{-3}, which is greater than one carrier per unit cell (75 nm thick film). Figure 2.5b displays the carrier mobility after 5 minutes of hydrogen plasma exposure. On average, the mobility is $\mu = 0.183$ cm^2•V^{-1}•s^{-1}. This low mobility is likely due to the large number of carriers and ionic disorder present in the thin film.

2.4 Optical properties of hydrogen plasma exposed BST thin films

The hydrogen plasma exposed BST thin films are optically transparent in the visible region (Fig. 2.6b). Figure 2.6a shows that the 5 minute hydrogen plasma exposed BST thin film exhibits a clear Drude response due to conducting carriers.

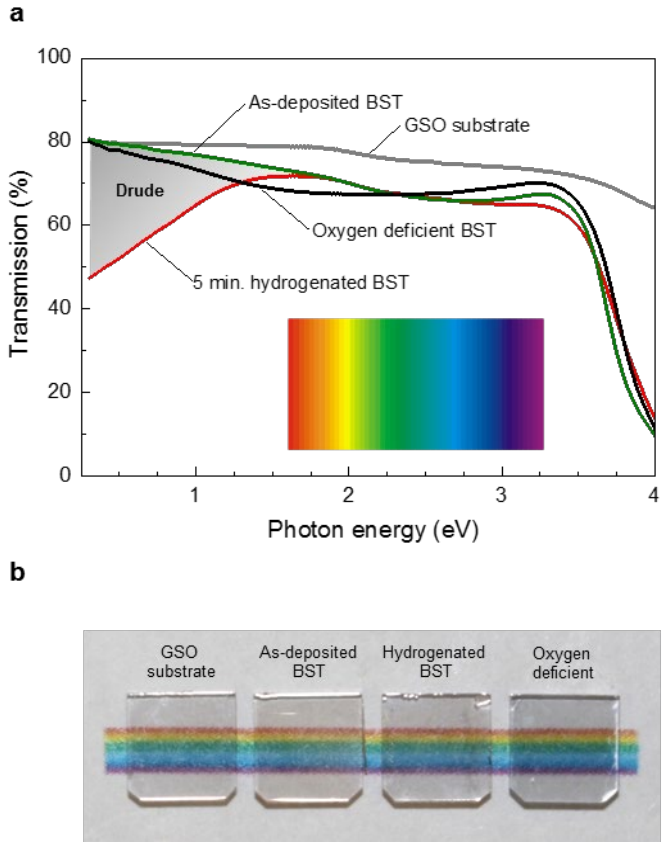

Figure 2.6 Visible light transmission of the BST thin films. a, transmission spectra of the as-deposited, oxygen deficient, and 5 minute hydrogenated BST thin films. The GSO substrate spectra (gray curve) is shown for comparison. The gray region indicates the apparent onset of Drude conductivity. b, photograph comparing the various BST thin films and GSO substrate from a. Notice the increased absorption of the oxygen deficient thin film as compared to the hydrogen plasma exposed thin film. The hydrogenated, as-deposited, and GSO substrate show little difference in visible light transmission.

However, its plasma frequency is lower than the onset of the visible region ($\omega_p <$ 12905.02 cm^{-1}), allowing the samples to be as transparent as the as-deposited thin film or bare substrates (Fig. 2.6b). It is noteworthy that although hydrogen plasma exposure induces ionic disorder and strongly-correlated electrons, it does not deteriorate the optical

transparency in the visible region. Thus, hydrogen plasma exposure does not add light-absorbing impurity bands or defects such as oxygen vacancies[19,20,46,77,78] (Fig. 2.6a). However, this is not the case for the amorphous BST thin films on glass, as shown in Figure 2.7.

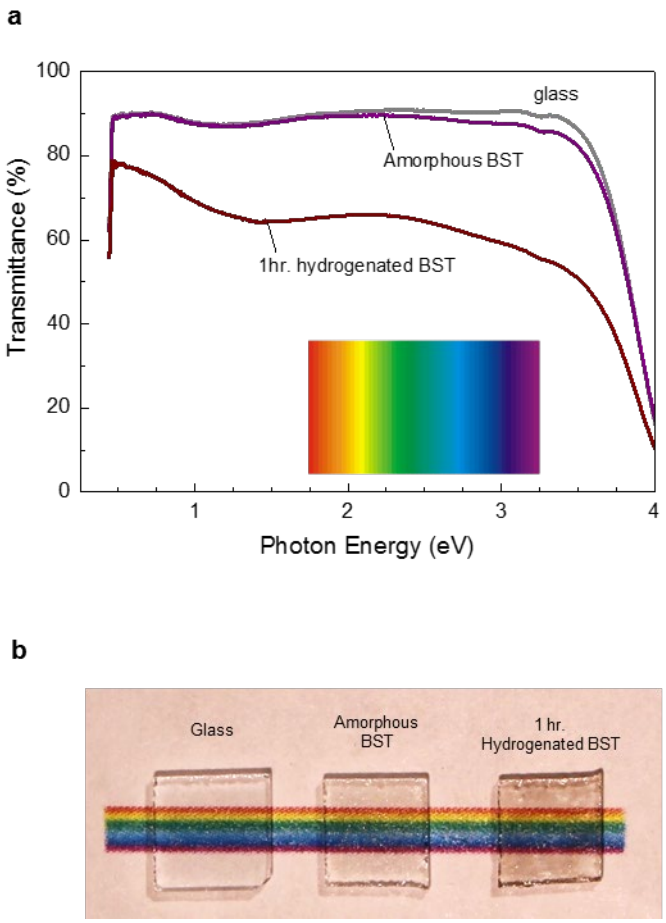

Figure 2.7 Transmittance of the amorphous BST thin films deposited on glass. a, transmission spectra of the as-deposited and 1 hour hydrogenated amorphous BST thin films. The glass substrate spectra (gray curve) is shown for comparison. b, photograph comparing the amorphous BST thin films and glass substrate from a. The hydrogenated thin film shows a difference in visible light transmission as compared to the as-deposited thin film.

Before hydrogenation, a 20 nm thick film of amorphous BST is nearly as transparent as the borosilicate glass substrate (See Fig. 2.7b). After 1 hour of hydrogenation, the thin

film is very absorbing in the visible region and displays insulating behavior at low temperatures (See Fig. 2.2 and Table 2.1).

From the transmittance data, we can estimate the TCO Figure of merit (FOM) as $\Phi = \frac{T^{10}}{R_{\square}} = 1.0 \times 10^{-3}\ \Omega^{-1}$ where T is the transmittance at 550 nm and $R_{\square}$ is the sheet resistance (See Supplementary Information for further calculation details)[85]. The FOM of our samples has a similar order of magnitude with that of SVO, as expected for a TCO with strongly correlated electrons, despite the ionic disorder introduced during hydrogen plasma exposure[2,46,52,77,78]. The comparison with other TCO FOM's is listed in Table 2.2.

Table 2.2 Figure of Merit values for various TCO's

Material	Transmittance[4]	Sheet Resistance (Ω/□)[6]	Figure of Merit (Ω^{-1})
Hydro. BST (5 min. 75 nm)[1]	0.893[5]	323	1.0×10^{-3}
$SrVO_3$ (50 nm)[2]	0.625[5]	7	1.3×10^{-3}
Cd_2SnO_4 (1 μm)[3]	0.84	3.1	5.2×10^{-2}
In:SnO_2 (2 μm)[3]	0.83	2.4	7.1×10^{-2}

1 This work
2 L. Zhang *et al.* Nat. Mat. **15**, 204 (2016).
3 G. Haake Journ. Appl. Phys. **47**, 4086 (1976).
4 Value taken at 550 nm
5 See Section 2.4 for calculation details
6 Value taken at Room Temperature

The FOM of our samples has a similar order of magnitude with that of SVO, as expected for a TCO with strongly correlated electrons, despite the ionic disorder introduced during hydrogen plasma exposure[2,46,52,77,78].

As hydrogen plasma exposure time increases, the optical spectra indicate that this BST thin film system undergoes phase transitions. The optical conductivity ($\sigma_1(\omega)$) of the thin films is presented in Fig. 2.8.

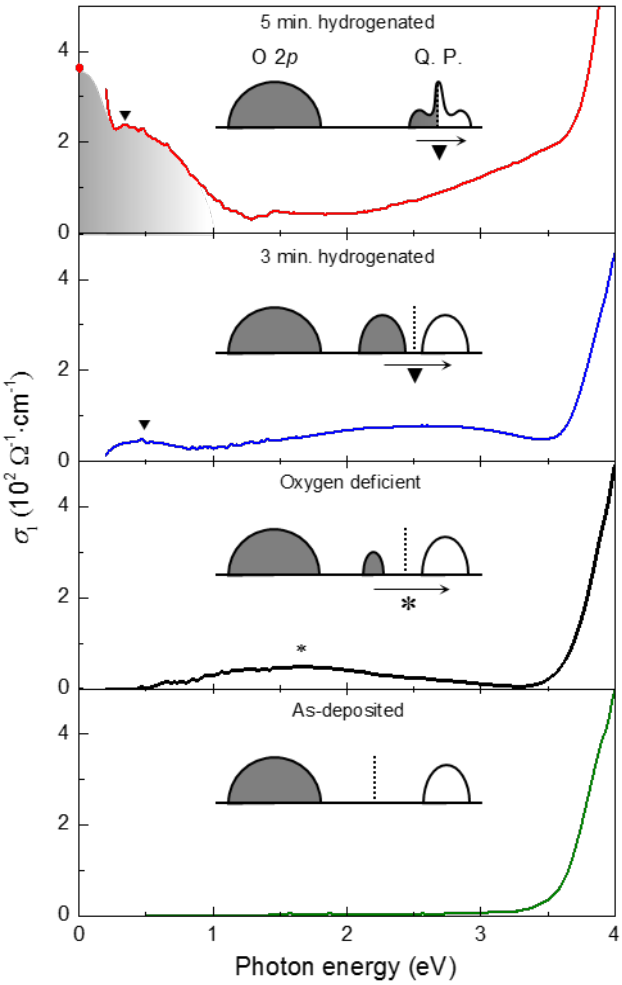

Figure 2.8 Optical conductivity for the as-deposited, oxygen deficient, 3 minute hydrogenated, and 5 minute hydrogenated samples (bottom to top). The ▼ indicates the transition generated by conducting quasiparticles added y hydrogen plasma exposure. The red dot in the 5 minute hydrogenated sample data at 0 eV is the room temperature conductivity. The gray region indicates the Drude response of the 5 minute hydrogenated thin film. The * peak is the added mid-gap state due to the extra defects present in the oxygen deficient thin film from deposition conditions. The insets are band diagrams extrapolated from the optical conductivity data.

The optical parameters are obtained by fitting the transmittance and reflectivity of the thin films, which are presented in Fig. 2.9.

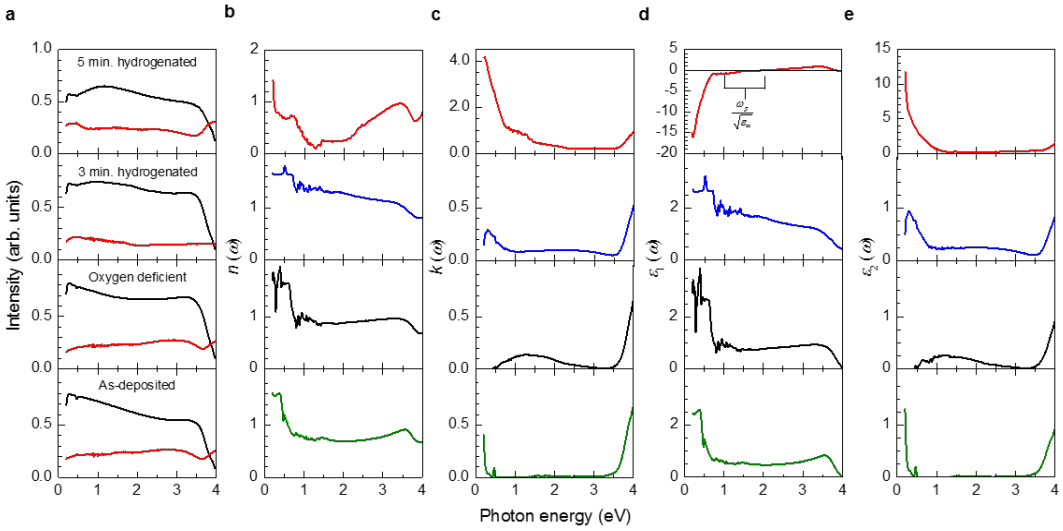

Figure 2.9 Optical parameters for hydrogenated BST thin films. a, normalized transmittance (black lines) and reflectivity (red lines) for the 5 minute hydrogenated, 3 minute hydrogenated, oxygen deficient, and as-deposited BST thin films. The transmittance and reflectivity are normalized to 1=100 % intensity (fully transmitting or fully reflecting). b, index of refraction (n) for the thin films. c, extinction coefficient (k) for the thin films. d, real part of the dielectric constant (ε_1) for the thin films. The range of $\frac{\omega_p}{\sqrt{\varepsilon_\infty}}$ is shown by the bracket for the 5 minute sample. e, imaginary part of the dielectric constant (ε_2) for the thin films.

The as-deposited BST thin film shows only the charge-transfer transition, from O_{2p} to Ti_{3d}, above 3.5 eV. The oxygen deficient BST thin film also shows a broad peak (*) centered around 1.7 eV, which is due to a mid-gap state near the Ti_{3d} conduction band[46]. It is noteworthy that despite this mid-gap state, the oxygen deficient BST thin film remains very insulating. As a BST thin film undergoes hydrogen plasma exposure for 3 minutes, a low energy excitation (▼) forms. This peak red shifts after 5 minutes of hydrogen plasma exposure. The previously mentioned Drude response (See Fig. 2.6a)

with a nearby excitation is indicative of electron-electron interactions at atomic sites that are broadened by electron hopping, indicating quasiparticle based conductivity that demonstrates the presence of a correlated metallic state[30,32]. From the Drude response of the 5 minute hydrogen plasma exposed sample, we can extract the effective carrier mass using the carrier concentration from the Hall measurements (n = 1.67×10^{22} cm^{-3}, see Fig. 2.5a). We find the effective carrier mass to be between $3.5m_e$ and $15.2m_e$ using $\omega_p^2 = \frac{4\pi ne^2}{m^*}$, where ω_p ranges from 16937.64 cm^{-1} to 8065.54 cm^{-1}. We give a range for the plasma frequency due to the uncertainty generated by the broad ▼ peak as observed in Fig. 2.8. Our range of effective mass is similar to other strongly-correlated and heavily electron doped titanates, i.e. $Sr_{(1-x)}La_xTiO_3$ (from $2.0m_e$ to about $10m_e$ as x ranges from 0.1 to 1) and hydrogen reduced $SrTiO_3$ ($4.9m_e$ when n = 5.3×10^{20} cm^{-3})[21,86]. Thus, the enhanced effective mass of the conducting carriers in the hydrogen plasma exposed BST thin films combined with the *MR* observations (See Fig. 2.3) confirm that the carriers are strongly-correlated.

2.5 XPS properties of BST thin films

The X-ray Photoemission spectra (XPS) of our BST thin films display the effects of hydrogen plasma exposure on the electronic properties of our BST thin films. The XPS spectra for the 5 minute plasma hydrogenated, 30 second plasma hydrogenated, as-deposited, and oxygen deficient thin films are displayed in Fig. 2.10.

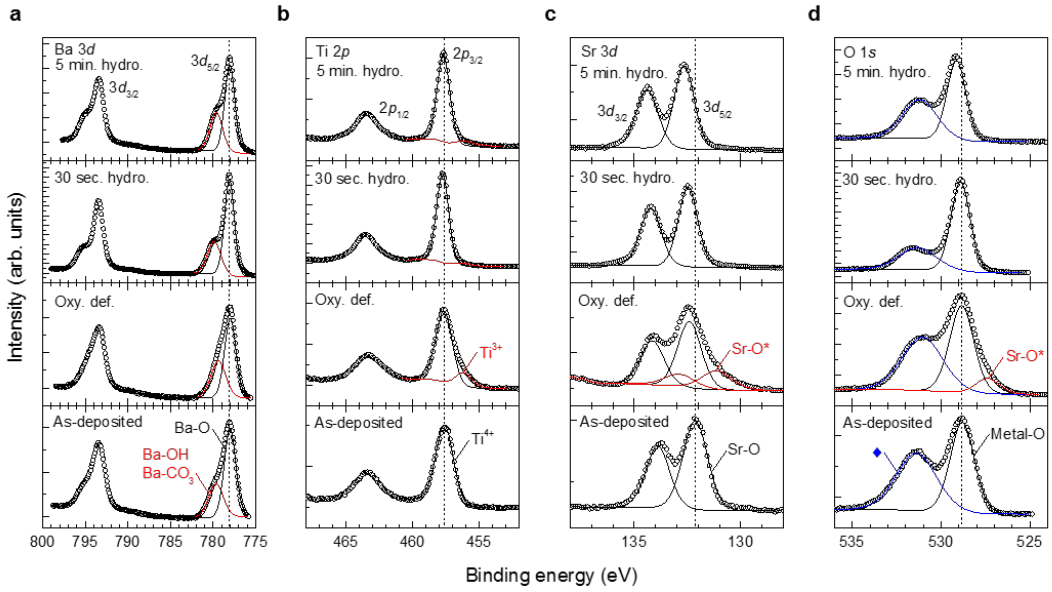

Figure 2.10 XPS spectra of the BST thin films. a, X-ray photoemission spectra (XPS) of the Ba 3d(3/2) and Ba 3d(5/2) peaks. The raw spectra is indicated by the open black circles. The black fit line indicates Ba-O bonding and the red fit line indicates Ba-OH/BaCO3 bonding. b, XPS for the Ti 2p(1/2) and Ti 2p(3/2) peaks. Ti4+ and Ti3+ bonding are indicated by the black and red line fits, respectively. c, XPS for the Sr 3d(3/2) and Sr 3d(5/2) peaks. Sr-O bonding is fit by the black line. The Sr-O* bonding in the oxygen deficient sample is fit by the red line. d, XPS for the O 1s peak. Metal-O bonding is fit by the black line. Sr-O* bonding in the oxygen deficient sample is fit by the red line. The ♦ peak, which is due to oxygen vacancies, hydroxide, and carbonates is fit by the blue line. The vertical dotted lines indicate the position of the as-deposited Ba-O, Ti4+, Sr-O, and Metal-O peaks. The linear intensity scale is 20000 counts.

All data has been normalized using the carbon C 1*s* spectra (284.5 eV)[87,88]. The energy and full width half maximum of all deconvoluted peak fits is recorded in Table 2.3.

Table 2.3 XPS peak positions for the BST thin films

Sample	Ba-OH $BaCO_3$	Ba-O	Ti^{4+}	Ti^{3+}	Sr-O[2]	Sr-O* (Sr 3*d*)[2]	♦[3]	Metal-O[4]	Sr-O* (O 1*s*)
Hydro. BST (5 min.)	779.6 (1.8)[1]	778.1 (1.4)	457.7 (1.1)	456.2 (1.7)	132.7 (1.1)	-	531.2 (2.3)	529.1 (1.3)	-
Hydro. BST (30 sec.)	779.9 (1.8)	778.1 (1.4)	457.7 (1.1)	456.3 (1.5)	132.5 (1.1)	-	531.4 (2.4)	528.9 (1.3)	-
As-deposited	779.8 (2.0)	778.0 (1.6)	457.6 (1.6)	-	132.1 (1.2)	-	531.4 (2.7)	528.8 (1.6)	-
Oxygen deficient	779.4 (2.0)	778.0 (1.6)	457.6 (1.5)	456.2 (1.5)	132.4 (1.3)	132.1 (1.7)	531.1 (2.7)	528.8 (1.6)	527.4 (1.6)

1 Full width half maximum (FWHM) for each peak is in parenthesis.
2 Value of the lower binding energy peak.
3 Peak due to oxygen vacancies, hydroxide, and carbonate.
4 Metal-O includes Ti^{4+}, Ba-O, and Sr-O bonding.

Ba $3d_{5/2}$ spectra in Fig. 2.10a can be deconvoluted into peaks representing Ba-OH and $BaCO_3$ (779.8 eV) bonding[89], as well as Ba-O (778.0 eV) bonding[90]. The Ti 2*p* spectra displaying the Ti $2p_{1/2}$ and the Ti $2p_{3/2}$ peaks is shown in Fig. 2.10b. The 5 minute plasma hydrogenated, 30 second plasma hydrogenated, and oxygen deficient samples all display peaks that can be attributed to both Ti^{4+} bonding (457.6 eV)[91] and Ti^{3+} bonding (456.2 eV)[92]. In contrast, the as-deposited thin film can only be fit by a single Ti^{4+} peak. Figure 2.10c shows the Sr 3*d* spectra displaying the Sr $3d_{3/2}$ and Sr $3d_{5/2}$ peaks. The plasma hydrogenated (132.7 eV for 5 minute plasma hydrogenated and 132.5 eV for 30 second plasma hydrogenated) and oxygen deficient (132.4 eV) Sr-O peaks shift to a higher binding energy as compared to the as-deposited thin film (132.1 eV)[93]. The oxygen deficient spectra can be further deconvoluted into a lower energy peak that we denote as Sr-O*(131.1 eV), which may indicate the presence of hole doping in the oxygen deficient thin film[94]. The O 1*s* spectra is displayed in Fig. 2.10d. Only the 5 minute plasma hydrogenated thin film displays a peak shift to a higher binding energy for the Metal-O bond (529.1 eV) as compared to the 30 second plasma hydrogenated (528.9

eV), oxygen deficient (528.8 eV), and as-deposited (528.8 eV) thin films. Further, the intensity of the ♦ peak (531.4 eV), which can be attributed to oxygen vacancies[95], hydroxides[96], and carbonates[97] present in the thin films, is reduced for the plasma hydrogenated thin films. It also is noteworthy that the O 1*s* spectra of the oxygen deficient thin film includes the Sr-O* peak (527.4 eV), as discussed above[94].

X-ray Photoelectron Spectroscopy (XPS) shows that the observed transparent conductivity is due to a novel conduction mechanism. There is significantly less Ti^{3+} bonding generated by hydrogen plasma exposure as compared to the amount of Ti^{3+} bonding in the oxygen deficient sample (See Fig. 2.10b)[92]. This observation agrees with the data in Fig. 2.6 and Fig. 2.8, which shows that hydrogen plasma exposure does not reduce visible region transparency via the addition of oxygen vacancies (Ti^{3+}). Thus, the conduction mechanism in our hydrogen plasma exposed BST thin films is not due to oxygen vacancies introduced during exposure. However, as the hydrogen plasma exposure time increases, the main peak in the Sr 3*d* and O 1*s* spectra shift to a higher binding energy with respect to the as-deposited BST thin film (See Supplementary Figs. 2.10c and 2.10d). This shift can be understood as an increase in the Fermi energy due to electron doping[88,98,99]. This fact indicates that hydrogen plasma exposure has increased the number of electrons in the BST thin film, which is consistent with the resistivity and transport measurements (See Fig. 2.1a and Fig. 2.5a). It is noteworthy that the intensity of the ♦ peak is reduced with respect to the Metal-O peak in the O 1*s* spectra following hydrogen plasma exposure (See Fig. 2.10d). In general, the ♦ peak is attributed to oxygen vacancies[95], hydroxides[96], and carbonates[97] present in a material. The decreased intensity of the ♦ peak is unexpected for a system that has been exposed to hydrogen. In

fact, an increase in the intensity of this peak in other hydrogen exposed materials has been shown to have a direct effect on the reported electronic properties[46-50,52,77,78]. Hence, the small amount of Ti^{3+} bonding, the indication of electron doping, and the decrease in the amount of OH bonding combined with our previous observations on the structural, transport, and optical properties demonstrate that the conduction mechanism of the upper amorphous-like region is different from that of other hydrogen exposed systems[20,42,44-47,52,77,78,86,98]. However, the crystalline region below the amorphous-like layer (See Fig. 1b) also contributes to the observed transport properties (See Supplemental section "Conducting properties of insulating BST"). In order to fully probe the electronic properties of both of these regions, we suggest that secondary ion mass spectroscopy (SIMS) be taken to determine the chemical composition[48-50,55] in this unique system.

Further information can be gathered on these unique BST thin films by considering the structural and surface properties. Following these considerations, a discussion of the dielectric constant of these hydrogen plasma exposed thin films follows.

2.6 Structural Properties of BST thin films

X-ray characterization of our BST thin films show the effects of hydrogen plasma exposure and oxygen vacancies on the structural properties of our samples. Figure 2.11a displays the 2θ-ω scans of our as-deposited, 2 minute hydrogenated, 5 minute hydrogenated, and oxygen deficient thin films, respectively.

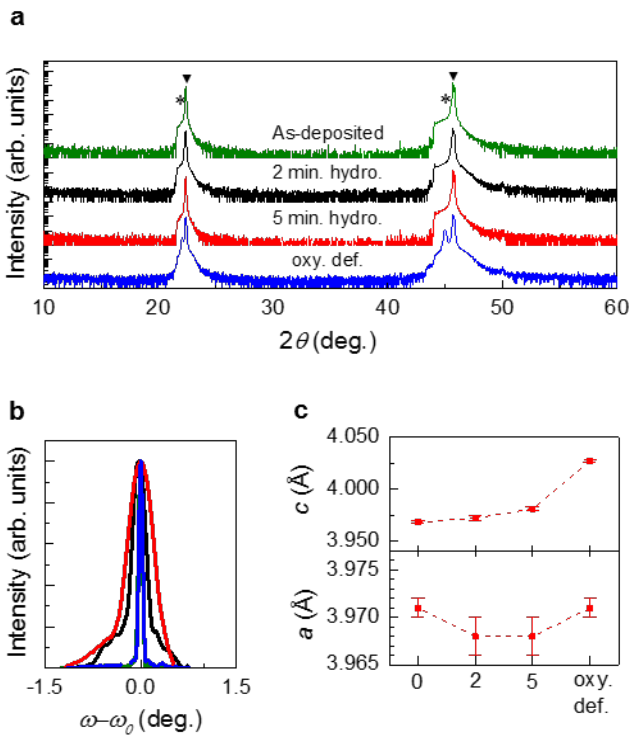

Figure 2.11 Structural properties of hydrogenated BST thin films. a, 2θ-ω scan of the as-deposited, 2 minute, 5 minute, and oxygen deficient BST thin films. The ▼ denotes the 110_O and 220_O $GdScO_3$ substrate peaks. The * indicates the 001_C and 002_C oxygen deficient BST thin film peaks. b, rocking curves for the as-deposited (green), oxygen deficient (blue), 2 minute hydrogenated (black), and 5 minute hydrogenated (red) BST thin films taken from the RSM's in Figure 2.1c. c, out-of-plane (*c*, top panel) and in-plane (*a*, bottom panel) lattice constants for the BST thin films in calculated from the RSM's in Figure 2.1c.

The substrate 110_O and 220_O peaks are denoted by ▼. The * indicates the 001_C and 002_C oxygen deficient BST thin film peaks. It is noteworthy that the BST thin film peaks cannot be observed in a 2θ-ω scan before or after hydrogen plasma exposure. Figure 2.11b displays the thin film rocking curves extracted from the reciprocal space maps (RSM) in Fig. 2.1c. The as-deposited and oxygen deficient thin films display similar rocking curves (FWHM=0.058) showing that both are high-quality epitaxial thin films[74].

After 2 minutes and 5 minutes of hydrogen plasma exposure, the rocking curves increase to 0.217 and 0.327 respectively, indicating that hydrogen plasma exposure has added a large amount of ionic disorder[46,77,78]. Figure 2.11c shows the evolution of the in-plane (*a*) and out-of-plane lattice constants (*c*). The in-plane lattice constants are the same for the as-deposited and oxygen deficient samples (3.971 ± 0.001 Å). However, the hydrogen plasma exposed thin films show a small reduction in *a*, with both having a value of 3.968 ± 0.002 Å. Due to the diffuse spread, our estimated in-plane constant value has a large error bar for the hydrogen plasma exposed samples and may actually be closer to the value observed in the unhydrogenated samples. As for the out of plane lattice constants, there is a continuous increase from the as-deposited (3.968 ± 0.001 Å), to the hydrogenated (3.972 ± 0.002 Å for 2 minutes of hydrogen plasma exposure, 3.981 ± 0.002 Å for 5 minutes of hydrogen plasma exposure), and finally, to the oxygen deficient (4.027 ± 0.001 Å) thin film. Intriguingly, hydrogen plasma exposure increases the out-of-plane lattice constant by +0.1% for the 2 minute hydrogen plasma exposed sample and +0.33% for the 5 minute hydrogen plasma exposed sample, while the addition of oxygen vacancies increases it by +1.49%. Further, metal hydride exposed thin films show a decrease in the out-of-plane lattice constant (i.e. –0.02% for $SrTiO_3$)[44] while ionic liquid gated thin films show an increase (i.e. up to +3.3% for $SrRuO_3$)[50]. These results further confirm the unique nature of these hydrogen plasma exposed BST thin films.

2.7 Surface properties of the BST thin-films

The surface of the BST thin films display the effects of hydrogen plasma exposure. Figure 2.12a shows a 3 x 3 μm^2 scan of a single-terminated atomically-flat GSO substrate[70].

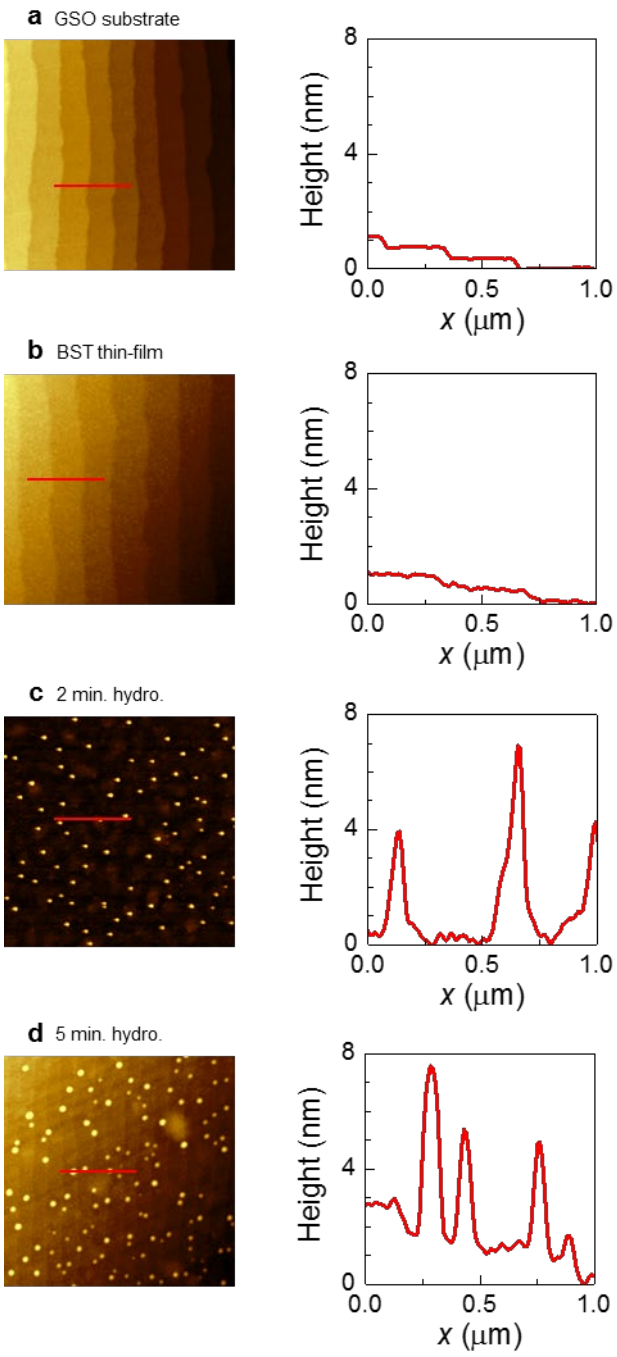

Figure 2.12 Surface properties of hydrogen plasma exposed BST thin films. a, GSO substrate with corresponding line profile after annealing. b, 75 nm thick BST thin film after deposition. c, BST thin film after 2 minutes of hydrogen plasma exposure. d, BST thin film after 5 minutes of hydrogen plasma exposure. All scans are 3x3 μm^2.

Immediately after deposition, the BST thin film displays step terrace growth in Fig. 2.12b. After hydrogen plasma exposure, the formation of hills occurs for both the 2 minute and 5 minute hydrogen plasma exposure samples (See Figs. 2.12c and 2.12d). These hills are probably due to the presence of $BaCO_3$ and Ba-OH on the surface of the thin film, which can also appear in as-deposited thin films a few weeks after thin film deposition. These hills similarly form on $SrTiO_3$ substrates a few days after high temperature annealing[68,100,101].

2.8 Calculation of static dielectric constant from Mott Criterion

The dielectric constant of the hydrogenated BST thin films is reduced as compared to BST single crystals and thin films. Figure 2.13 shows the estimated static dielectric constant for hydrogenated BST thin films.

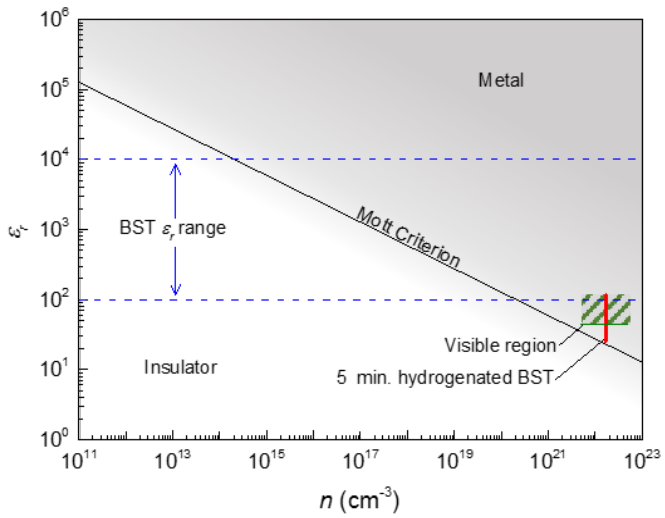

Figure 2.13 Estimated static dielectric constant for hydrogenated BST thin films. The Mott Criterion (solid black line) is plotted for the static dielectric constant (ε_r) vs. carrier concentration (n). Materials with values ε_r and n that fall below the Mott Criterion are predicted to show insulating behavior while those materials with values above the line are predicted to show metallic behavior. The dotted blue lines indicate the static dielectric constants for various BST single crystals and thin films.[39,56,60-62] The vertical red line indicates the estimated dielectric constant based on the effective carrier mass for the 5 minute HPE BST thin films. The green line and hashed region indicate plasma frequencies that are in the visible region.

The black line gives the Mott Criterion[81], which is:

$$n^{-1/3} \sim 4a_H \tag{2.5}$$

where n is the carrier concentration and a_H is the Bohr radius given by:

$$a_H = \frac{4\pi\varepsilon_r\varepsilon_0\hbar^2}{m_e e^2} \tag{2.6}$$

where ε_r is the static dielectric constant of the material. We choose m_e in the general case to set a lower bound on the transition from an insulator to a metal. Substituting (2.6) into (2.5) and solving for ε_r, we find:

$$\varepsilon_r \sim \frac{m_e e^2}{8\pi\varepsilon_0 \hbar^2} n^{-1/3} \tag{2.7}$$

which is the equation of the black line. Materials with values of ε_r and n below this line are predicted to show insulating properties whereas values above this line are predicted to show metallic properties[81]. The two horizontal blue lines are ε_r values for both single crystal BST (higher values) and BST thin films (lower values)[39,56,60-62]. Naively, it would seem that doping n~10^{18} cm^{-3} carriers into a BST thin film where ε_r~10^3 should generate a metallic conductor, as high dielectric constant oxides, such as $SrTiO_3$, tend to be more prone to metallic conductivity[1]. However, BST does not become conducting upon conventional doping or the addition of oxygen vacaincies[40]. However, the dielectric constant of the BST fthin films may be reduced by hydrogen exposure. To estimate this reduction, we use the following approximation from P. A. Cox[1]:

$$n^{-1/3} \sim 4a_0 \tag{2.8}$$

where

$$a_0 = \frac{a_H' \varepsilon_r}{m^*/m_e} \tag{2.9}$$

with m^* as the effective carrier mass. a_H' is given by:

$$a_H' = \frac{4\pi\varepsilon_0 \hbar^2}{m_e e^2} \tag{2.10}$$

and equals 53 pm. Thus, substituting (2.9) into (2.8) and solving for ε_r,

$$\varepsilon_r \sim \frac{m^*}{m_e a_H'} n^{-1/3} \tag{2.11}$$

Equation (2.11) is used to generate the vertical red line in Figure 2.12 by setting $n = 1.67 \times 10^{22}$ cm^{-3} and varying m^* from $3.5m_e$ to $15.2m_e$ as estimated from the Drude conductivity in Section 2.4. As shown, our BST thin films display about an order of magnitude reduction in dielectric constant, particularly when considering effective masses that give a plasma frequency (ω_p) below the onset of the visable region (~1.6 eV or ω_p=12905 cm^{-1}, giving m^*=6.0m_e). It is reasonable to make this assumption since the hydrogenated thin films still transmit visable light (See Figure 2.6b). Thus, plasma hydrogenation reduces the dielectric constant in BSt along with the introduction of a novel conduction mechanism.

2.9 Summary

In summary, the first observation of transparent conductivity in BST thin films via short-term hydrogen plasma exposure has been shown. These transparent conducting states are generated by the interplay of ionic disorder and strongly correlated carriers. The structural, transport, optical, and electronic properties demonstrate that a new type of conducting mechanism could be responsible for this unique transparent conducting state, which warrant further experimental and theoretical investigation. This unique state reveals a new approach for studying the interplay of strongly-correlated electrons in non-equilibrium systems. Furthermore, these novel states also indicate a new roadmap for the development of low cost TCO's via short-term hydrogen exposure of insulating dielectric oxides. This work will be submitted to Nature Materials for publication[23].

CHAPTER 3. CONDUCTING $LaAlO_3/SrTiO_3$ HETEROINTERFACES ON ATOMICALLY FLAT SUBSTRATES PREPARED BY DEIONIZED-WATER

We have investigated how the recently-developed water-leaching method for atomically-flat $SrTiO_3$ (STO) substrates affects the transport properties of $LaAlO_3$ (LAO) and STO heterointerfaces. Using pulsed laser deposition at identical growth conditions, we have synthesized epitaxial LAO thin films on two different STO substrates, which are prepared by water-leaching and buffered hydrofluoric acid (BHF) etching methods. The structural, transport, and optical properties of LAO/STO heterostructures grown on water-leached substrates show the same high-quality as the samples grown on BHF-etched substrates. These results indicate that the water-leaching method can be used to grow complex oxide heterostructures with atomically well-defined heterointerfaces without safety concerns.

3.1 Introduction

Preparation of atomically-flat surfaces of substrates is an important step to successfully fabricate well-characterized epitaxial thin films and heterointerfaces. For example, the atomically flat TiO_2-terminated $SrTiO_3$ surface[3-6] is the key for creating the high-mobility two-dimensional election gas (2DEG) at $LaAlO_3/SrTiO_3$ (LAO/STO) heterointerfaces, which show intriguing multichannel conduction[102-105], interfacial superconductivity[7], ferromagnetism[8,9], and for developing electronic devices and sensors[106-108]. The atomically-flat surfaces of $SrTiO_3$ (STO) single crystal substrates are usually achieved by an acid-based chemical etching procedure[63,109,110] followed by thermal-annealing. For example, buffered-hydrofluoric acid (BHF), which is used in silicon semiconductor research and industry for removing SiO_2, has been used widely for

making atomically-flat STO substrates[63,100,109-112]. Recently, we have shown that a *non-acidic* deionized-water leaching method (water-leaching) is as effective at generating single-terminated atomically-flat STO substrates[68]. The water-leaching method can remove effectively SrO, which is a hydrophilic compound[64,67,68,100,101,112-114], from the STO surface. Since 6-14% of fluorine impurities can be doped into the STO surface during the BHF-etching procedure[64,65], water-leaching eliminates not only the safety concerns of acidic etchants but also possible impurity doping on the surface.

In this Chapter, we report that the water-leaching method creates heterointerfaces that have the same high-quality as those generated through the BHF-etching method. We have investigated the LAO/STO 2DEG as a representative model system requiring atomically well-defined STO substrates. By *simultaneously* depositing $LaAlO_3$ (LAO) thin films under the same conditions on two STO substrates, which are prepared by the water leaching and BHF-etching methods, respectively, we have observed that there is no noticeable difference between the two heterointerfaces regarding their structural, transport, and optical properties.

3.2 Methods

We have synthesized LAO/STO heterointerfaces on atomically-flat surfaces of (100)-oriented STO substrates that are prepared by using either the water-leaching[68] or BHF-etching methods[63]. All substrates (purchased from CrysTec GmbH) are sliced into two pieces ($5 \times 2 \times 1$ mm^3), are annealed at 1000 °C in ambient conditions for 1 hour, which forms a dual-terminated step-and-terrace structure, and each piece is leached (etched) for 30 s in deionized-water (BHF), respectively. Substrates are again annealed

at 1000 °C for 2 hours, which effectively forms atomically-flat single-terminated surfaces, reducing the overall surface roughness. The final step of substrate preparation is to once again leach in deionized-water or etch in BHF as before in order to eliminate possible strontium oxides or strontium hydroxides segregated on the surface[68]. A full discussion of the water leaching method can be found in Appendix A.1. Atomic Force Microscopy (Park XE-70) is employed to ensure the formation of single-terminated atomically-flat substrates before deposition and to confirm thin film surface quality after deposition. Epitaxial LAO thin films of various thickness (5 – 60 unit-cells) are deposited on the STO substrates using pulsed laser deposition with a laser fluence (KrF excimer, λ = 248 nm) of 1.6 J/cm^2, a substrate temperature of 700 °C, and pO_2 of 10^{-6} Torr. *In situ* reflection high energy electron diffraction (RHEED) is utilized to monitor the number of unit cells of LAO deposited. The grown samples are cooled naturally for 2 hours to room temperature at a higher oxygen partial pressure (10 mTorr) so that the films have proper oxygen stoichiometry. There is no clear systematic thickness dependence of LAO thin films on their transport properties, as reported previously[115]. Thus, here we focus our discussion on the results obtained from the 5, 25, and 30 unit-cell LAO samples. Structural quality of the thin films is characterized using X-ray diffractometry (Bruker D8 Advance). Optical transmission spectra is taken at room temperature using a Fourier-transform infrared spectrometer (FT-IR) (for spectra regions between 50 meV and 0.6 eV) and a grating-type spectrophotometer (for spectra regions between 0.5 and 6 eV). Transport properties are measured using a Physical Property Measurement System (Quantum Design) with conventional four-probe and Hall geometries. Hall measurements are taken at various temperatures at a maximum

magnetic field of 9 T. Electrical contacts are made using aluminum wire attached with indium solder, which gives access to the 2DEG present at the heterointerface.

3.3 Results and discussion

LAO thin films deposited on the water leached STO substrates show the same thin film quality as BHF-etched substrates. Figure 3.1a depicts a 3×3 μm^2 atomic force microscopy (AFM) topography scan of a water-leached STO substrate with respective line profile below.

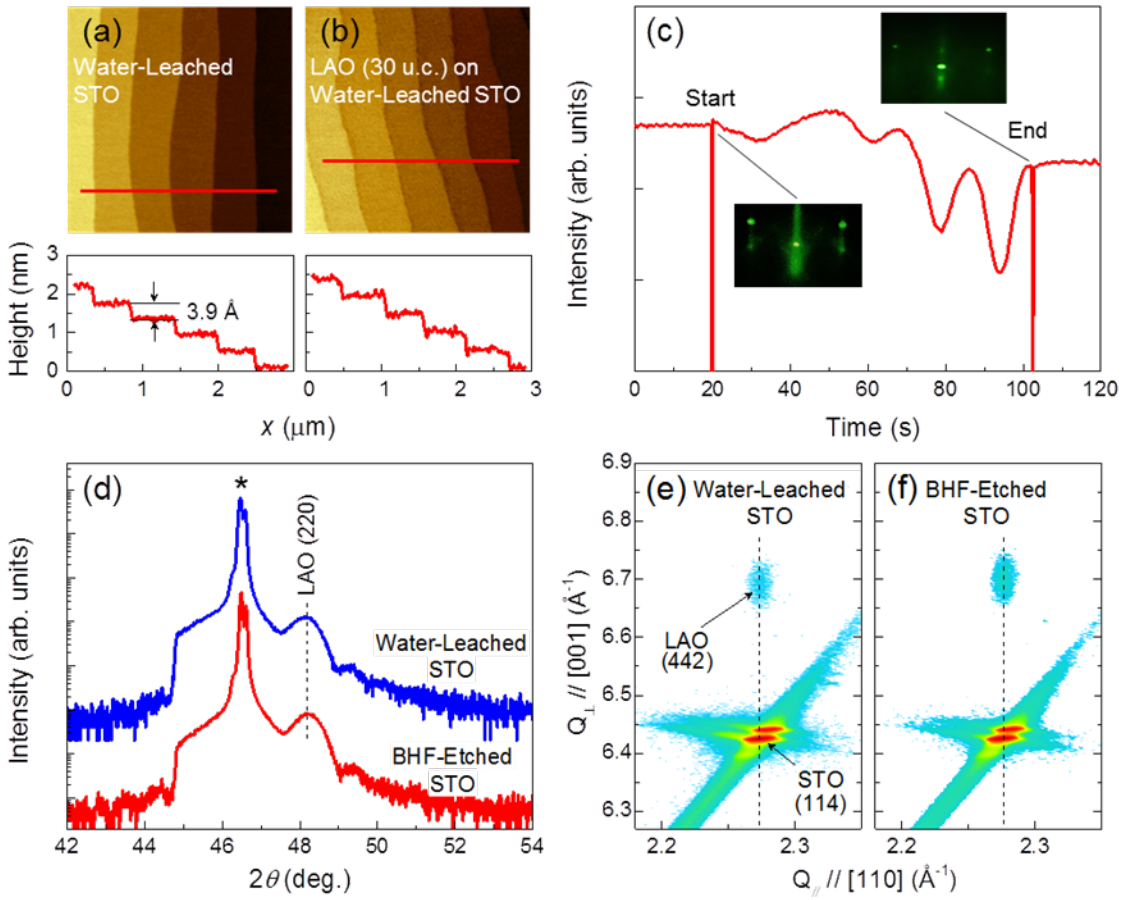

Figure 3.1 Crystal properties of LAO films deposited on water-leached and BHF-etched STO substrates. 3 × 3 μm^2 AFM topography of a water-leached substrate (a) before and (b) after deposition of a 30 unit-cell LAO thin film. The red lines correspond to the line profiles shown below each AFM scan. (c) RHEED intensity oscillations of the 5 unit-cell water-leached LAO thin film deposition on a water-leached STO substrate. The insets show the RHEED pattern at the beginning and end of the thin film growth. (d) X-ray θ-2θ scans of the 30 unit-cell water-leached sample (blue) and BHF-etched sample (red). The asterisk (*) indicates the STO substrate (200) reflection. X-ray reciprocal space maps near the STO (114) reflection for the 30 unit-cell LAO thin films deposited on (e) water-leached and (f) BHF-etched substrates. Note that both LAO thin films are coherently strained.

As indicated in the line profile, the substrate has a step height of 3.9 Å, which is the lattice constant of cubic STO. Figure 3.1b displays the same sample as in (a) after

deposition of a 30 unit-cell LAO film. Both images show single-terminated atomically-flat step terraces before and after deposition. Figure 3.1c displays the RHEED intensity oscillations for the 5 unit-cell thick LAO film deposited on the water-leached substrate. The insets show the RHEED patterns at the beginning and end of film deposition, which, other than a change in intensity, do not display any noticeable changes. The high quality of the LAO films is confirmed further by the X-ray θ-2θ scans, as shown in Fig. 3.1d for the 30 unit-cell thick films. The peak position of the (220)-LAO plane does not depend on substrate preparation method. The X-ray reciprocal space maps near the (114)-STO reflection show that both LAO thin films exhibit coherent in-plane tensile strain with no evidence of strain relaxation, as shown in Fig. 3.1e for water-leached and Fig. 3.1f for BHF-etched samples.

The optical transmission spectra of both heterointerfaces show little qualitative difference in the range of 0.2 – 3.2 eV, demonstrating that their optical properties and electronic structures are quite similar regardless of substrate preparation method. Figure 3.2 illustrates the optical transmittance spectra of the 25 unit-cell LAO/STO grown on water-leached and BHF-etched substrates.

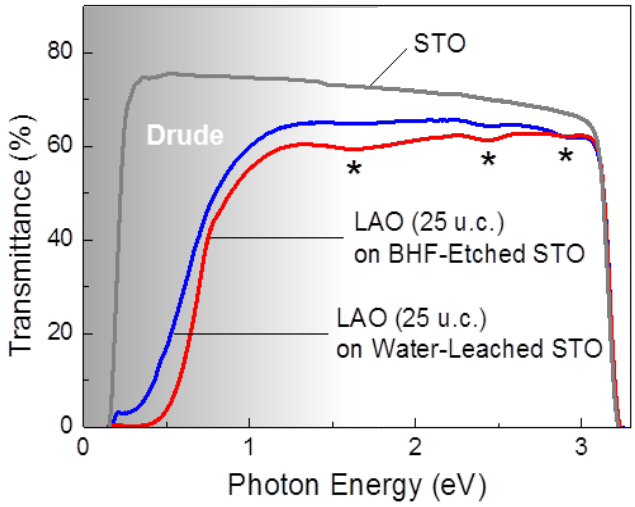

Figure 3.2 Optical transmittance spectra of 25 unit-cell LAO thin films grown on water-leached (blue) and BHF-etched (red) STO substrates. The STO substrate (grey) is shown for comparison. The asterisks (*) at 1.7, 2.4 and 2.9 eV indicate the optical absorptions due to oxygen vacancies. The shaded region below about 1.5 eV indicates the decrease of optical transmittance due to conducting Drude carriers. Two sudden drops of optical transmittance at 0.2 eV and 3.2 eV are due to the Reststrahlen band and the bandgap energy of STO, respectively.

Both spectra demonstrate clear Drude absorption due to conducting carriers, i.e. the decrease of optical transmittance, below about 1.5 eV. These transmittance spectra are consistent with the optical properties of LAO/STO heterointerfaces, as has been reported previously.[102] The three dip structures near 1.7, 2.4, and 2.9 eV are commonly observed in LAO/STO heterostructures and reduced STO crystals. The absorption at 1.7 eV increases as STO crystals are reduced, hence it is related to the oxygen vacancy level[20]. The dip structures at 2.4 eV and 2.9 eV are observed regardless of free carrier concentration, and they may originate from the excitation of electrons trapped by oxygen vacancies, i.e. F_1 centers[19].

The sheet resistance of both heterointerfaces has similar behavior down to low temperatures, regardless of substrate preparation method. Figure 3.3 shows the sheet resistance as a function of temperature for the LAO/STO heterointerfaces for the 5 unit-cell and 30 unit-cell LAO layers.

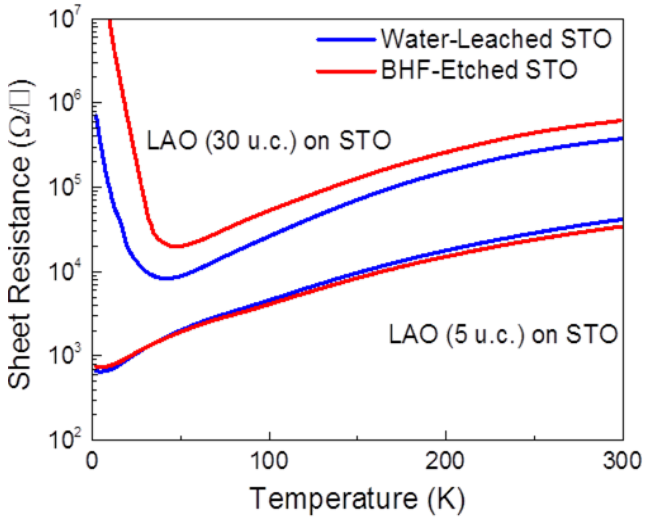

Figure 3.3 Temperature dependence of the sheet resistance of the 5 and 30 unit-cell LAO thin films grown on water-leached (blue) and BHF-etched (red) STO substrates.

The sheet resistance of the same LAO thickness is qualitatively identical despite the use of two different methods of substrate preparation. It is noteworthy that the 30 unit-cell LAO/STO samples display metal-insulator transitions at around 40 K while the 5 unit-cell LAO/STO samples are overall metallic. This behavior has been reported previously: the resistivity of LAO/STO heterointerfaces with thicker LAO layers can be larger than that of thinner samples, which may be due to structural reconstructions at the LAO/STO interface[115].

The heterointerfaces also have comparable carrier concentrations and mobilities. The results of the Hall measurements for the metallic 5 unit-cell LAO/STO heterointerfaces are displayed in Figs. 3.4a and 3.4b.

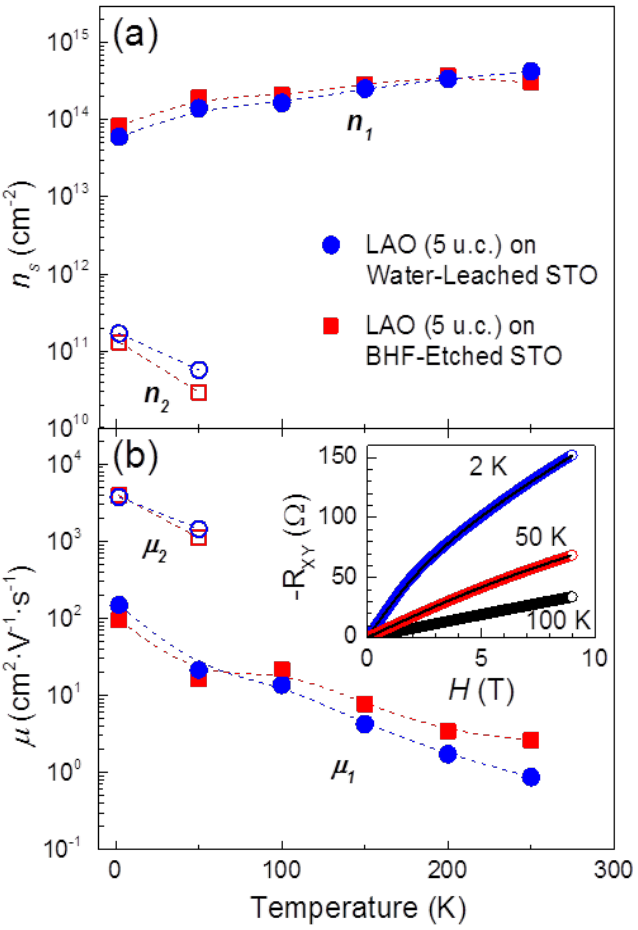

Figure 3.4 Temperature dependence of the (a) sheet carrier concentration and (b) mobility for the 5 unit-cell LAO/STO heterointerfaces. The filled circles (squares) indicate the high-density low-mobility carriers and open circles (squares) indicate the low-density high-mobility carriers for samples grown on the water-leached (BHF-etched) STO substrates. The dotted lines in (a) and (b) are guides for the eye. The inset in (b) shows the Hall resistance as a function of magnetic field at 2, 50, and 100 K for the sample grown on a water-leached STO substrate. The black lines are the two-carrier model fits.

Sheet carrier concentration (n_s) and mobility (μ) of the heterointerfaces prepared on the two kinds of STO substrates are similar regardless of preparation method. The values of n_s and μ compare well to those of other conducting LAO/STO 2DEG's where similar deposition conditions were used[3-5,115]. Further, room temperature n_s exceeding or near 10^{13}-10^{14} cm^{-2} are observed in most LAO/STO 2DEG's when the pO_2 of deposition is below 10^{-5} Torr[3-5,115]. Thus, as in most low-pO_2 LAO/STO heterointerfaces, oxygen vacancies play a role in the heterointerfacial conductivity. It is noteworthy that below 100 K we observe the non-linear Hall effect due to multi-channel electron conduction as shown in the inset of Figure 3.4b as has been seen previously[103-105]. This effect can be fitted by a two-band model, assuming the same sign for the charge carriers[13]. Thus, we can write the Hall coefficient, $R_H = \frac{R_{XY}}{B}$, as $R_H = \left(\frac{1}{e}\right)\frac{n_1\mu_1^2+n_2\mu_2^2+(n_1+n_2)\mu_1^2\mu_2^2B^2}{(n_1\mu_1+n_2\mu_2)^2+(n_1+n_2)^2\mu_1^2\mu_2^2B^2}$[13,27,116,117]. We can rewrite this equation of four unknown parameters as an equation of two unknown parameters, $R_H = \frac{R_0+R_\infty\mu_*^2B^2}{1+\mu_*^2B^2}$, where μ_* and R_∞ are fitting parameters with R_0 being $R_H(B=0)$. Using the zero field resistivity, $R_{XX} = (en_1\mu_1 + en_2\mu_2)^{-1}$, we can find the low-density-high-mobility (LDHM) (n_2 and μ_2) and high-density-low-mobility (HDLM) (n_1 and μ_1) carriers using $A = \frac{1}{2}(\frac{R_0}{R_{XX}} + \mu_*)$, $\mu_1 = A + (A^2 - \frac{\mu_*R_\infty}{R_{XX}})^{1/2}$, $\mu_2 = A - (A^2 - \frac{\mu_*R_\infty}{R_{XX}})^{1/2}$, $C = \frac{\mu_1(\mu_*-\mu_2)}{\mu_2(\mu_1-\mu_*)}$, $n_1 = \frac{1}{eR_\infty(1+C)}$, and $n_2 = \frac{C}{eR_\infty(1+C)}$[116-118]. The model fits at 50 and 2 K are shown by the black lines in the inset of Figure 3.4b. As stated above, neither the LDHM nor the HDLM display any differences based on substrate preparation. According to Chambers *et al.*, the BHF-etching method might result in a few percent of fluorine doping into STO, which can

provide 4×10^{13} cm^{-2} to 1×10^{14} cm^{-2} extra carriers[65]. Figure 3.4a, however, shows that n_s for both samples is very similar in the whole measurement temperature range. As for changes in μ, Chambers *et al.* also suggests that the fluorine atoms, acting as impurity sites, would increase the scattering rate, thereby reducing the overall μ of any heterointerface[65]. However, the μ of the two kinds of 5 unit-cell 2DEG samples shows little or no difference, as displayed in Fig. 3.4b. Thus, fluorine doping does not appear to alter the electronic properties of oxygen deficient conducting LAO/STO heterointerfaces.

Surface hydrogen doping does not seem to change the heterointerfacial conducting properties. As suggested by Hatch *et al*., hydrogen doping due to BHF-etching should contribute some difference in the conducting properties. However, Hatch *et al*. also states that water-leaching generates oxygen vacancies at the surface[64]. Further, our samples are heated up to 700 °C at a pO_2 of 10 mTorr. For comparison, T. Sakaguchi *et al.* has demonstrated that around ~350 to ~450 °C is enough to cause hydrogen to escape metal hydride exposed perovskite oxide single crystals[43]. The majority of the interfacial hydrogen has probably left the surface before or during thin film deposition. Hence, a study on the conducting heterointerface generated at deposition temperatures below ~300 °C may show a meaningful difference. Such heterointerfaces have been generated by depositing amorphous layers on STO substrates at room temperature[119].

3.4 Summary

LAO/STO heterointerfaces grown on water-leached and BHF-etched STO substrates show similar structural, optical, and electronic properties. Based on these results, the water-leaching method produces not only atomically-flat single-terminated

surfaces of STO but also high-quality heterointerfaces of complex oxides. Recently, various oxide heterointerfaces grown on STO substrates such as $LaTiO_3/SrTiO_3$[10,12,13], $LaVO_3/SrTiO_3$[116,120], $LaMnO_3/SrTiO_3$[14], $GdTiO_3/SrTiO_3$[121], $NdAlO_3/SrTiO_3$[122], and $NdGaO_3/SrTiO_3$[122,123] have demonstrated intriguing electronic reconstructions, interfacial superconductivity, and magnetic ordering. Hence, the use of the water-leaching method promotes research on future oxide electronics by providing a safe way to prepare atomically-flat complex-oxide substrates. This work has been published in Scientific Reports[24].

CHAPTER 4. CONCLUSIONS AND FUTURE OUTLOOK

4.1 Conclusions for hydrogen plasma exposed BST thin films

Short-term hydrogen plasm exposure of BST thin films represent a new direction in the generation of transparent conducting oxides. Our results demonstrate that short-term hydrogen plasma exposure can lead to the formation of a novel correlated metallic state through the addition of strongly-correlated conducting carriers and ionic disorder. Hence, in the following section, we suggest some future research directions based on these intriguing results.

4.2 Implications of transparent conducting BST thin films

The exploration of plasma hydrogenation on thin films of $SrTiO_3$ (STO) and $BaTiO_3$ (BTO) has yet to be completed. Hosono *et al*., Bouilly *et al*., and T. Yajima *et al.* have shown that hydrogenation can generate conducting states in STO and BTO thin films[42,44,45]. However, there has not been any exploration of short-term hydrogen plasma exposure on these constituent materials, other than the results for a single crystal of STO shown in Figs. 1.2 and 1.6. An investigation of these materials on (110)-oriented $GdScO_3$ substrates may help to explain our results as discussed in Chapter 2. Further, we suggest (001)-oriented $(LaAlO_3)_{0.3}(Sr_2AlTaO_6)_{0.7}$ (LSAT) substrates as have been used for other strongly-correlated transparent conducting oxides and for hydrogenated BTO and STO thin films in the past[2,45,124]. Due to the compressive strain of the substrate on the thin film, these thin films could show ferroelectric behavior[124]. If short-term hydrogen plasma exposure of BTO and STO does not induce as much ionic disorder as is seen for BST, an enhanced carrier mobility near the ferroelectric phase transition may be

observed[28]. Hence, further research on the transparent conducting state discussed in Chapter 2 may also lead to the observation of a high mobility transparent conducting state.

The observation of the novel conducting state that forms in these BST thin films warrants further exploration. Typically, conductivity is expected to be generated via electron hopping from one B-site transition metal to another in a perovskite[1]. However, this is not true for the short-term hydrogen plasma exposed BST thin-films (See Section 2.5). Thus, further theoretical and experimental work is needed to understand this unique state. One experiment would be to consider thinner (20 nm or less) crystalline BST thin-films. An observation of a shorter (longer) hydrogen plasma exposure time can reveal a critical thickness to host these strongly-correlated transparent conducting states. Further, varying the amount of barium (Ba) and strontium (Sr) in the thin-films may show interesting results. Based on the XPS data in Fig. 2.10, it appears that oxygen and Sr are the primary contributors to the electronic properties observed in the upper amorphous-like regions of these BST thin films. Thus, by decreasing (increasing) the Ba content, the amount of hydrogen plasma exposure required for the onset of conductivity may be decreased (increased). Any decrease in plasma hydrogenation time may reduce the amount of ionic disorder introduced during hydrogenation and improve carrier mobility and increase conductivity. Further, increasing the Ba content may make the samples more insulating, as the Ba site does not appear to be electronically active in the upper amorphous-like regions (See Fig. 2.10a). Samples with a high Ba content may prove to be useful to further our understanding of localized states in a non-equilibrium system.

4.3 Conclusions for conducting $LaAlO_3/SrTiO_3$ heterointerfaces

The similarity in the conducting properties of both heterointerfaces is not surprising considering the deposition conditions used[24]. Thus, hydrogen doping from BHF may be removed during substrate annealing before sample deposition. Regardless, Chapter 3 has shown that the water leaching method not only generates a single-terminated atomically-flat STO substrate, but that it also allows for the formation of heterointerfaces that have the same structural, optical, and transport properties as those generated by BHF-etching. However, in order to possibly observe the effects of hydrogen and fluorine on the interfacial properties, we suggest the future research below.

4.4 Implications of similar conducting properties and water leaching

The similar conducting properties observed in Chapter 3 demonstrate that both hydrogen and fluorine do not contribute to the transport properties of our LAO/STO heterointerfaces due to our deposition conditions. Thus, a future study that focuses on the properties of conducting heterointerfaces deposited at temperatures below 300 °C could shed light on this system[119]. Further, as shown in Fig. 3.3, insulating heterointerfaces may show meaningful differences in their transport properties, especially near the metal-to-insulator transition. Finally, other conducting heterointerfaces, such as $LaTiO_3/SrTiO_3$[10,12,13], $LaVO_3/SrTiO_3$[116,120], $LaMnO_3/SrTiO_3$[14], $GdTiO_3/SrTiO_3$[121], $NdAlO_3/SrTiO_3$[122], and $NdGaO_3/SrTiO_3$[122,123] can be considered. These systems may retain the effects of either hydrogen or fluorine on the conducting properties of the heterointerfaces. By combining these methods, the observation of mobility or conductivity differences in these heterointerfaces may be more likely.

The implications of water leaching on the thin film oxide community have been far reaching. The method has been used to generate single-terminated atomically flat STO substrates for many thin films and heterostructures[125-127]. The water leaching method has also been scrutinized in a few cases as well[128,129]. In general, oxide thin film groups tend to use the water leaching method when they wish to avoid the investment in costly safety equipment required for BHF-etching, since both methods tend to generate substrates with similar properties[68].

4.5 Conclusions regarding the effects of hydrogen on insulating titanates

In conclusion, the effects of hydrogen on insulating titanates have shown two interesting results. First, hydrogen plasma exposure can be used to generate unprecedented transparent conductivity. Second, surface hydrogen at a conducting oxide heterointerface may have an effect on the conducting and transport properties of that heterointerface. In both cases, future work is needed to understand the true nature of hydrogen in the generation of these intriguing properties and novel conducting states.

APPENDICES

APPENDIX A PREPARATION OF ATOMICALLY FLAT $SrTiO_3$ SURFACES USING A DEIONIZED-WATER LEACHING AND THERMAL ANNEALING PROCEDURE

We report that a deionized-water leaching and thermal annealing technique can be effective for preparing atomically-flat and single-terminated surfaces of single crystalline $SrTiO_3$ substrates. After a two-step thermal-annealing and deionized-water leaching procedure, topography measured by atomic force microscopy shows the evolution of substrates from a rough to step-terraced surface structure. Lateral force microscopy confirms that the atomically-flat surfaces are single-terminated. Moreover, this technique can be used to remove excessive strontium oxide or hydroxide composites segregated on the $SrTiO_3$ surface. This acid-etchant-free technique facilitates the preparation of atomically-aligned $SrTiO_3$ substrates, which promotes studies on two-dimensional physics of complex oxide interfaces.

A.1 Introduction

Recently, intriguing electronic properties have been discovered at the interfaces of complex oxides: a high-mobility two-dimensional electron gas (2DEG) at the interface of $LaAlO_3/SrTiO_3$[3-6,130], which has been shown to exhibit both superconductivity[6] and ferromagnetism[8,9] as well as electronic reconstructions and superconductivity at the interfaces of $LaTiO_3/SrTiO_3$[10-13], $LaVO_3/SrTiO_3$[120], and magnetic ordering in $LaMnO_3/SrTiO_3$ superlattices[14]. Orbital reconstructions[15] and high-T_c superconductivity[16] in cuprite interfaces along with magnetoelectric[17] and strain-tuning[131]

effects in $LaMnO_3/SrMnO_3$ superlattices have also been observed. Studying interfacial phenomena of complex oxides provides important clues not only to understanding the physics of complex oxides but also to advancing oxide electronics[18].

Preparation of atomically-flat surfaces of substrates is an indispensable step to successfully prepare well-characterized samples and to achieve the intriguing electronic properties at the interfaces. Since the atomically-abrupt interfaces can be achieved only when substrates are flat, effective methods of preparing flat substrates cannot be overemphasized. Atomically-flat surfaces of strontium titanate ($SrTiO_3$) single crystals, which are by far the most widely used substrate in complex-oxide research, are typically achieved by using an acid-based etchant[63,109] and thermal-annealing. For example, the method based on buffered-hydrofluoric acid (BHF) etching, which is the same chemical etching procedure used in silicon semiconductor research and industry for removing SiO_2, resulted in atomically-flat $SrTiO_3$ substrates[63,109-112,132]. Owing to the safety issues of acidic etchants, these acid-based methods have been a barrier against promoting active research of interfacial properties of complex oxides.

In this appendix, we show that a *non-acidic* deionized (DI)-water treatment and thermal annealing technique can be effectively used to prepare atomically-flat and single-terminated surfaces of $SrTiO_3$ substrates. The perovskite $SrTiO_3$ has two possible surface terminations along the (100) direction: SrO and TiO_2. We note that the SrO layer of $SrTiO_3$ has an ionic bonding nature, which is in contrast with the covalent bonding of SiO_2. Thus, water (H_2O) might be effective to chemically remove the SrO layer since SrO is a water-soluble material[101,112,113,133-135]. By combining two thermal annealing steps before and after DI-water treatment, our process successfully removes SrO

terminated layers as well as what are most likely segregated strontium oxide or hydroxide islands from the surface.

A.2 Methods

We have taken commercially available $SrTiO_3$ (100) and $SrTiO_3$ (111) single crystalline substrates (Crystec GmbH) and prepared them by annealing at 1000ºC for 1 hr. (1^{st} thermal annealing) in air. Substrates are then rinsed with DI water (Resistance > 15 MΩ, pH = 7.0 ± 0.2) via agitation for about 30 seconds at room temperature. Finally, the substrates are annealed again at 1000ºC (2^{nd} thermal annealing) for 1 hr. in air. The surfaces of the substrates are characterized through the leaching and annealing process using an Atomic Force Microscope (Park XE-70).

A.3 Results

Figure A1 illustrates surfaces of a $SrTiO_3$ (100) substrate that is prepared by the process at each step.

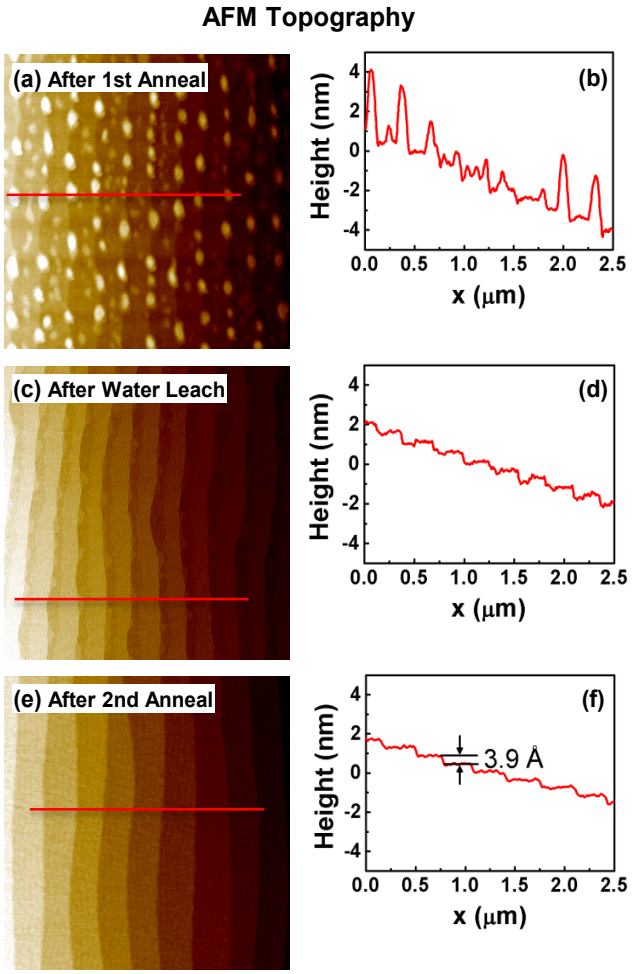

Figure A1 Surface evolution of a $SrTiO_3$ (100) substrate through the deionized-water leaching and thermal-annealing process. (a) AFM topography after 1st thermal annealing with line profile (b). (c) AFM topography after water-leaching with line profile (d). (e) AFM topography after 2nd thermal annealing. As shown in (f) the final substrate is atomically flat with rms roughness of ~0.2 Å. Scan area is 3 × 3 μm^2. Reproduced from Connell, J. G., Isaac, B. J., Ekanayake, G. B., Strachan, D. R. & Seo, S. S. A. Preparation of atomically flat SrTiO3 surfaces using a deionized-water leaching and thermal annealing procedure. *Applied Physics Letters* **101**, 251607 (2012), with the permission of AIP Publishing.

Figure A1a shows the sample after the 1st annealing step. The rather large islands formed on the sample surface are due to strontium oxide or hydroxide segregation[100]. Figure A1c supports this hypothesis as the water soluble SrO and SrO hydroxide islands have been removed by DI-water treatment. It is noteworthy that there are half-unit-cell high step-

terraces as shown in Figs. A1c and A1d. Figure A1e and A1f show the sample following the 2nd thermal annealing. An atomically-flat surface has been produced by the process with a step height of 3.9 Å and roughness of approximately 0.2 Å.

Clearly, an atomically-flat substrate surface has been produced. However, it is not clear just from AFM topography that this sample is single-terminated. Thus, Lateral Force Microscopy (LFM) has been employed as has been previously used on $SrTiO_3$ and other perovskite surfaces[31,32] to check surface-termination. Figure A2a (A2b) and A2c (A2d) show the AFM (LFM) images before and after the 2nd thermal annealing, respectively.

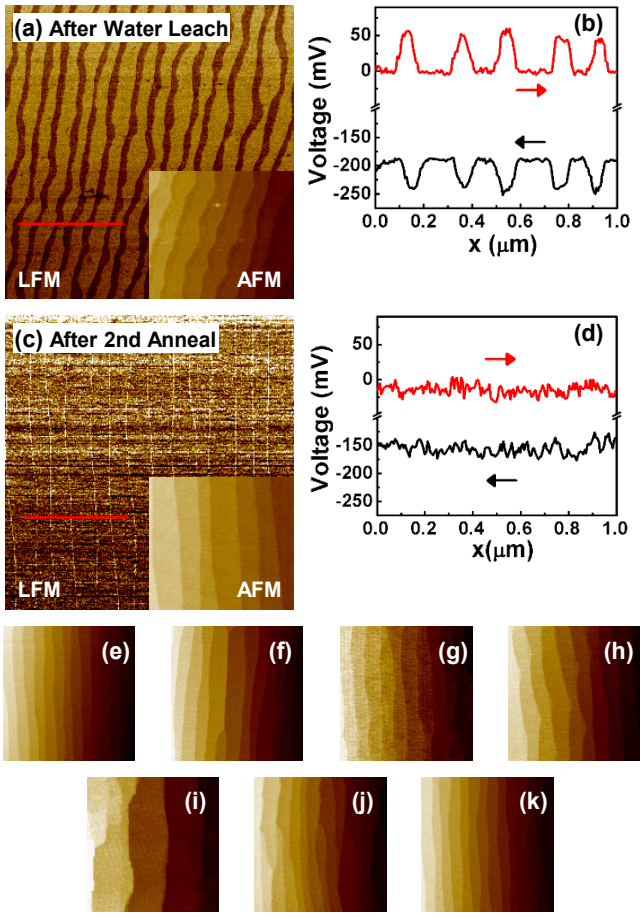

Figure A2 (a) Lateral Force Microscopy (LFM) of a $SrTiO_3$ (100) substrate after DI-water leaching and (b) the line profiles of LFM signal trace and retrace (arrows). (c) The same substrate after 2nd annealing and (d) the line profile of LFM signal trace and retrace (arrows). The insets in (a) and (c) show corresponding AFM topography. (e)-(k) Examples of $SrTiO_3$ (100) substrates that are tested by using the same leaching and annealing process. All substrates are atomically flat and singly-terminated. Scan area is 3 × 3 μm^2. Reproduced from Connell, J. G., Isaac, B. J., Ekanayake, G. B., Strachan, D. R. & Seo, S. S. A. Preparation of atomically flat SrTiO3 surfaces using a deionized-water leaching and thermal annealing procedure. *Applied Physics Letters* **101**, 251607 (2012), with the permission of AIP Publishing.

Note that the Fig. A2b LFM image shows the regions of non-uniform friction near the step edges which corresponds to the half-unit-cell deep regions in Fig. A2a. However, after its second annealing, Figures A2c and A2d show that the LFM topography shows

uniform frictional response, which implies that the substrate is single-terminated. We tested more substrates to see whether our method is reproducible: Figures A2e – A2k display AFM topography images of a few $SrTiO_3$ (100) substrates which have been treated through the same water-leaching and thermal annealing process. Atomically flat surfaces are obtained regardless of their step-terrace widths and miscut angles. Step-bunching is observed in some substrates. However, the step bunching is not due to our method but due to substrate crystallinity since we have observed similar step-bunching in BHF treated substrates as well.

We have shown that substrates that have been prepared via the water-leaching and thermal annealing process are both atomically-flat and single-terminated. However, surface-degradation due to SrO segregation or Sr out-diffusion has been observed in a few hours or days after the 2^{nd} annealing, as shown in Fig. A3a.

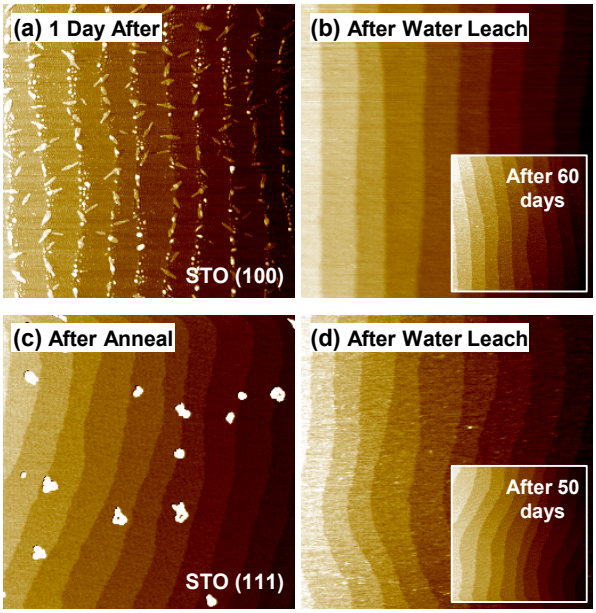

Figure A3 AFM topography images of (a) a $SrTiO_3$ (100) substrate 1 day after the second annealing and (b) after another DI-water leaching. The inset shows the same substrate 60 days later. (c) $SrTiO_3$ (111) substrate after the second annealing and (d) after DI-water leaching. The inset shows the same substrate 50 days later. Scan area is 3×3 μm^2. Reproduced from Connell, J. G., Isaac, B. J., Ekanayake, G. B., Strachan, D. R. & Seo, S. S. A. Preparation of atomically flat SrTiO3 surfaces using a deionized-water leaching and thermal annealing procedure. *Applied Physics Letters* **101**, 251607 (2012), with the permission of AIP Publishing.

SrO segregations are visible near the step-edges and similar surface-degradation has also been reported for BHF-etched and thermally annealed substrates[111,132]. Figure A3b shows that these degraded surfaces can be improved by another 30 second water-leaching step: The segregated SrO islands are removed and an atomically flat surface is recovered. The inset of Fig. A3b shows that the substrate preserves the surface even 61 days after the water-leaching step. LFM confirms that the surface is still single-terminated (data not shown). This implies that the final DI-water treatment results in rather chemically stable surfaces free from SrO segregation. We also tested our method on $SrTiO_3$ (111)

substrates, which have until now been typically prepared using BHF[110,136]. Figure A3c shows that $SrTiO_3$ (111) substrates also have SrO segregations on their surfaces after our process. However, after one more water-leaching step, SrO segregations have once again been removed and the surface is clean and atomically-flat as shown in Fig. A3d. The inset of Fig. A3d shows that the substrate surface is flat even 51 days after the treatment. Thus our method works for both $SrTiO_3$ (100) and (111) substrates.

A.4 Summary

In summary, atomically-flat single-terminated surfaces of $SrTiO_3$ (100) and (111) substrates were prepared using a water-leaching and thermal annealing technique. Furthermore, better chemically stable surfaces can be obtained when the final step in the process is water-leaching. While previously preparing this manuscript, we have learned of two publications[65,114] and a patent[113] where a warm (50 – 100 ºC) water bath and/or ultraviolet light exposure has been used to prepare $SrTiO_3$ substrates, which showed consistent results with ours. Our *acid-etchant-free* technique eliminates the safety issues of the acid-based etching process, which will promote the progress of research on interfacial physics of complex oxides.

APPENDIX B DESIGN AND CONSTRUCTION OF A PLD CHAMBER

As a necessary first step to the two projects discussed above in Chapter 2 and 3, I designed a vacuum chamber for pulsed laser deposition. An image of that chamber is shown in Fig. B1 and the layout of the chamber is given in Table B1.

Table B1 Vacuum chamber component location

Diameter of opening (in.)	Polar Angle (degrees)	Azimuthal Angle (degrees)	Focal Length (in.)	Description of use	Focal Point (in.)	Figure
8	0	0	11	Heater	0,0,0	B2a
8	90	0	11	Door	0,0,0	B2b
8	90	90	11	Viewport	0,0,0	B2b
8	90	180	11	Blank	0,0,0	B2c
8	90	270	11	Turbo Pump	0,0,0	B2b
8	180	90	11	Target Manipulator	0,0.5,0	B2c
6	45	45	11	Viewport	0,0,0	B2b
6	45	135	11	Blank	0,0,0	B2c
6	45	225	11	Blank	0,0,0	B2d
6	45	315	11	Viewport	0,0,0	B2a
4.5	45	270	13	Laser Port	0,0,-1	B2a
4.5	135	45	11	Blank	0,0,0	B2b
4.5	135	135	11	Blank	0,0,0	B2c
4.5	135	225	11	Blank	0,0,0	B2d
4.5	135	315	11	Blank	0,0,0	B2a
4.5	45	90	13	Blank Laser Port	0,0,-1	B2b
2.75	90	45	11	Blank	0,0,0	B2b
2.75	90	135	11	Blank	0,0,0	B2c
2.75	90	225	11	Nude Ion Gauge	0,0,0	B2d
2.75	90	315	11	N_2 Valve	0,0,0	B2a
2.75	70	45	11	Blank	0,0,0	B2b
2.75	70	135	11	Blank	0,0,0	B2c
2.75	70	225	11	Blank	0,0,0	B2d
2.75	70	315	11	Blank	0,0,0	B2a
2.75	110	45	11	Roughing Valve	0,0,0	B2b
2.75	110	135	11	Pirani Gauge	0,0,0	B2c
2.75	110	225	11	Viewport	0,0,0	B2d
2.75	110	315	11	Turbo Angle Valve	0,0,0	B2a
1.33	90	30	11	O_2 Leak Valve	0,0,0	B2b
1.33	90	120	11	Baratron Gauge	0,0,0	B2c

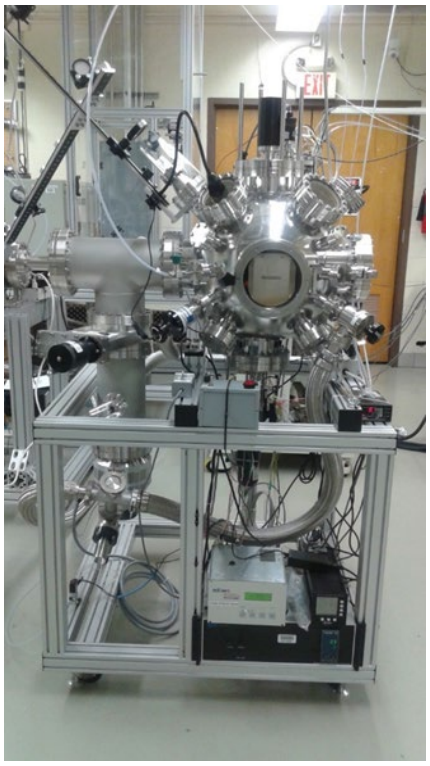

Figure B1 Image of PLD vacuum chamber in its current location. The chamber is set on a cart that has been built by Kurt Lesker, the same company that built the chamber body.

The final column of the table indicates the image in Fig. B2 where the components of the chamber are located, which will now be discussed in turn.

B.1 Components of a PLD vacuum chamber

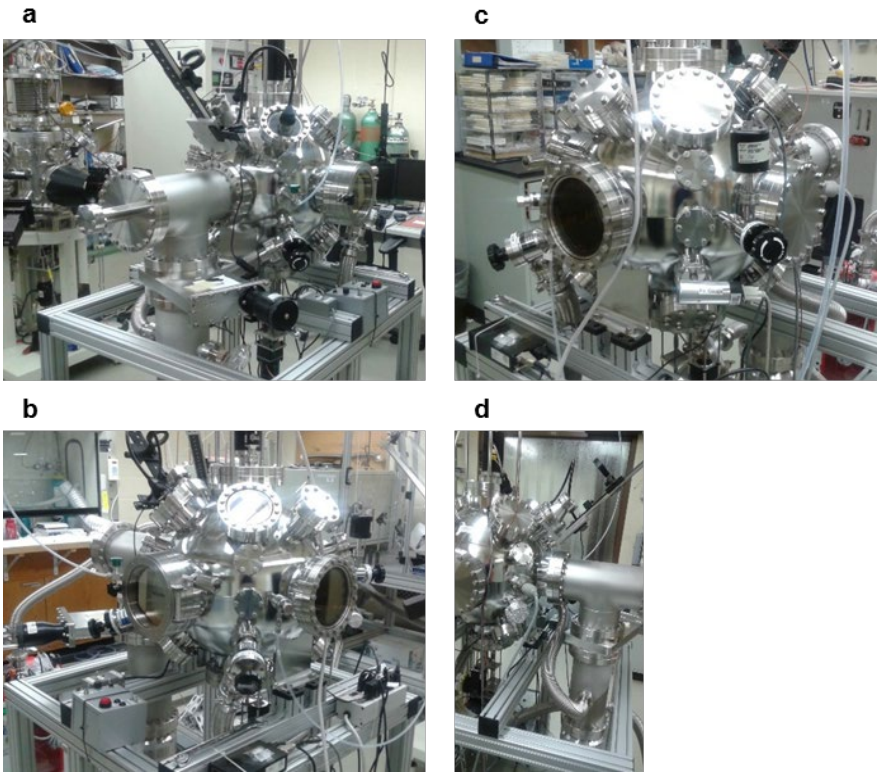

Figure B2 Views of the components of PLD chamber 2. a, view of the heater, laser port, viewport, N_2 valve, Turbo angle valve and Turbo gate value (top to bottom). Notice that the Turbo gate valve is connected to an 8 in. T with a 2 ¾ in. port on its end. Also note the Bayard-Alpert Ion gauge attached below the T. b, Blank laser port (former laser port in Figure 1.7), 6" viewport, 8 in. door, O_2 leak valve 8 in. viewport, and roughing angle valve (top to bottom). c, Baratron gauge, Pirani gauge, and target manipulator (top to bottom). d, nude ion gauge, 2 ¾ in. viewport (covered in foil) (top to bottom). The angle valve in a is connected to the Turbo pump via the bellows.

Figure B2a shows the locations of some of the major vacuum components of the chamber. Key to the generation of high vacuum (~10^{-6} to 10^{-8} Torr), a Turbomolecular (Turbo) pump is used that is backed by a roughing pump. Behind this Turbo pump, a pneumatic angle valve (Fore valve) ensures that the system does not experience oil backstreaming in the case of a power outage. This value automatically closes to ensure that no oil from the roughing pump can enter the Turbo pump or the vacuum chamber.

Further a leak valve that is located on the roughing pump ensures that the roughing line behind the Turbo pump is quickly brought up to room pressure (~760 Torr). A view of the Turbo pump and Fore value is located in Fig. B2 (lower left). A detailed view of the angle valve controller, roughing pump, and leak valve is located in Fig. B3.

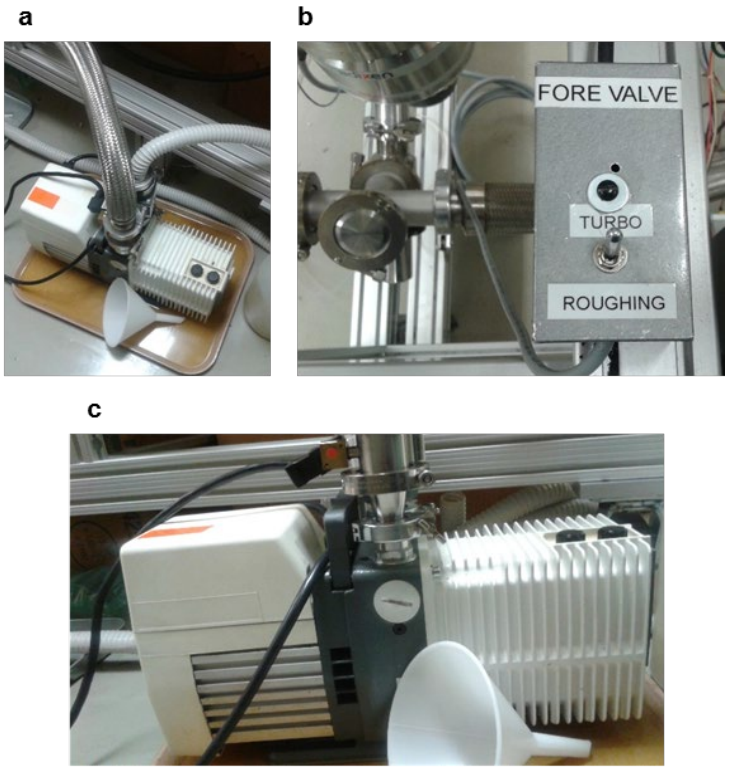

Figure B3 Roughing pump and Fore valve control. a, oil-based roughing pump. The plastic bellows is the pump exhaust, which goes into a fume hood. b, electronic fore valve control. The 4-way cross that connects the roughing line and the Turbo pump is shown on the left. The Fore valve is at the bottom of this cross. c, Side view of the oil-based rouging pump. The leak valve is the small black box with an electrical wire connection at the top of the image.

The Turbo pump is connected to the large T by a manually controlled gate valve. Further, the Turbo pump is connected to the Turbo angle valve by the bellows shown in Fig. B2d. These two connections allow for a large range of oxygen partial pressures (pO_2) (~10^{-6} Torr to 200 mTorr) to be used during deposition. For pressures of 1 mTorr

to 200 mTorr, the large gate valve is closed and all pressure control is done using the Turbo angle valve and the O_2 leak valve (See Fig. B2b). On the left side of this T is a blank 2 ¾ in. flange. This connection is there for the potential future addition of a Reflection High Energy Electron Diffraction system (RHEED). In fact, all of the 4 ½ in. ports that have a polar angle of 135° located in Figs. B2a through B2d are placed such that an Ellipsometry system could also be added in the future. The addition of these two components would allow for the *in situ* measurement of thin film thickness and electronic properties, respectively[137]. After deposition, the chamber is brought up to room pressure with the N_2 leak valve that is sourced with ultra-high purity nitrogen. Once the system is at air pressure, the Neocera heater (top of the chamber in Fig. B2a) can be safely removed. A detailed view of the electronic connections and of the adjustable properties of this block heater is shown in Fig. B4 below.

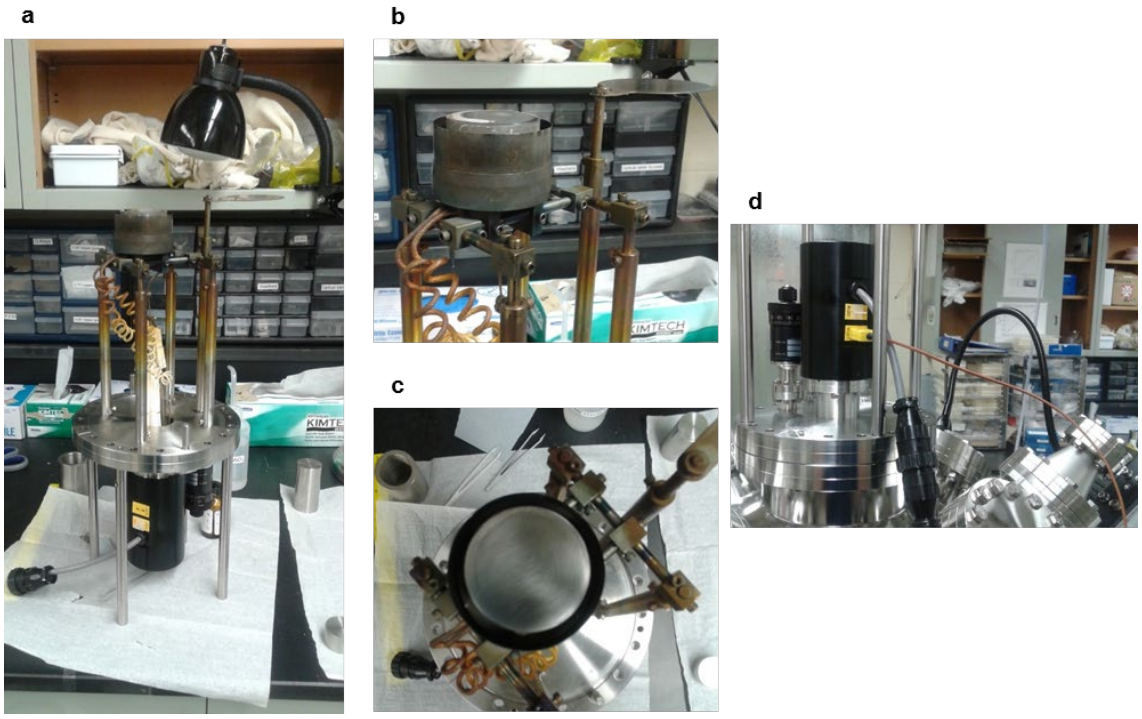

Figure B4 Close-up of Neocera block heater. a, the block heater outside of the vacuum chamber. The black lamp behind the heater is used for attaching substrates with silver paste. Note that the legs double as handles for moving the heater to and from the chamber. b, close-up of block heater. The substrate shield (right) has been moved away from the heater. Notice the set screws that allow for the heater to be adjusted vertically and horizontally. c, close up of heater plate from above. Substrates are placed in the center of the heater, where the heater temperature is within 10 °C of the set temperature. d, view of the electronics of the heater in the chamber. The thermocouple (yellow cord) and electronic connection (black cord) are shown. To the left is the rotator for the substrate shield. The laser port on the right will be discussed in Section B.3.

The laser port in Fig. B2a will be discussed in Section B.3.

Figure B2b shows more of the main components of the chamber. The door is primarily used to help in breaking vacuum pressures by opening its lock (black plastic star screw in Fig. B2a) while the N_2 valve is open. PLD targets are placed into the chamber via the door as well (See Fig. B5e). Some basic cleaning of the target

manipulator components can also be conducted through this door (See Fig. B5a). The O_2 leak valve is used in tandem with the Turbo gate valve and Turbo angle valve to set pO_2. The roughing angle valve is used to rough the vacuum from room pressure to about 50 mTorr. During this step, all Turbo valves including the Fore valve are closed (The Fore valve switch in Fig. B3b set to Roughing). This isolates the Turbo pump from damage as it is kept at full speed while sample processing, sample loading/unloading, and target loading/unloading occurs.

Figure B2c shows two of the gauges used to measure the pressure in the system. The Baratron gauge is a capacitance monometer that is accurate from 0.1 mTorr-1 Torr. It is used to precisely monitor pO_2 during deposition. Below this gauge is the Pirani gauge or Convection gauge. This gauge is accurate from room pressure to 1 mTorr. However, it is not as precise as the Baratron gauge in our pO_2 deposition range. The target manipulator shown at the bottom of Fig. B2c will be discussed in Section B.2.

Figure B2d shows the Nude Ion gauge. This gauge is used to measure the base pressure of the chamber to ensure that impurities have been removed via the vacuum pumps before deposition at our process pO_2, which can vary from sample to sample. It typically takes around 2-3 hours for the system to get below the minimum required pressure of 1×10^{-6} Torr. The lower port that is covered by foil is a small window port. This port has been used for illumination via an external light (now located on a 6 in. port in Fig. B2a) but has been covered to block UV laser light from exiting the chamber.

B.2 Target manipulator design

The target manipulator for chamber 2 underwent some redesign to improve it. Initially, the manipulator contained upper components that can be seen at the bottom of Fig. B5b. However, as shown in Fig, B5a, some of these components have been changed.

a

b

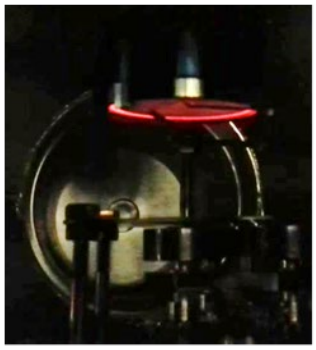

c

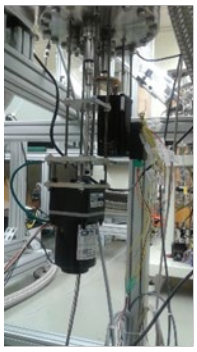

d

e

Figure B5 Changes in target manipulator and heater distance. a, current target manipulator design and heater-manipulator separation. The separation is around 2 in. b, former manipulator-heater separation. The separation is around 1 in., which would cause the two independent motors to move the system as one. c, Rotary motor (foreground) and stepper motor (background). Notice the 1.33 in. feedthrough on the 8 in. port at the top of the image. d, electronic motor control. The rotary motor is controlled by the switches and speed control on the left while the stepper motor is controlled on the right. By setting Pos. #1 and Pos. #2 and hitting the red Glide mode button, the stepper motor can be set to oscillate between two points while the target is rotated. e, 1 in. diameter single crystalline PLD target. Glide mode allows for the target to be used evenly, which lessens target surface polishing.

The reason for these changes is illustrated in the middle of Fig. B5b. The initial location of the substrate heater has been found to be too close to the target manipulator. While the heater is set to typical oxide thin film deposition temperatures (400 °C-800 °C), the independent motion of the motors would lock (see Figs. B5c and B5d for an image of the motors and motor control box, respectively), causing all target holders to rotate about the center of the manipulator. This would ruin sample deposition as the laser beam would hit multiple targets and the stainless-steel components of the chamber and target manipulator. The redesign of the upper components of the target manipulator is intended to move the components further away from the heat source, as shown in Fig. B5a. In fact a similar design principle has been used for the target manipulator located in our third chamber[138]. However, this locking of the target manipulator has been alleviated only through the use of the new adjustable heater, which is shown in Fig. B4b. The increased target manipulator-heater distance is shown in Fig. B5a. This increased distance has been enough to eliminate the motor locking problem that affected the use of this system in the past.

B.3 Laser beam path and sample deposition

Due to the addition of chamber 3, the laser beam path of chamber 2 has been adjusted. Figure B6a shows chamber 2 in its original location.

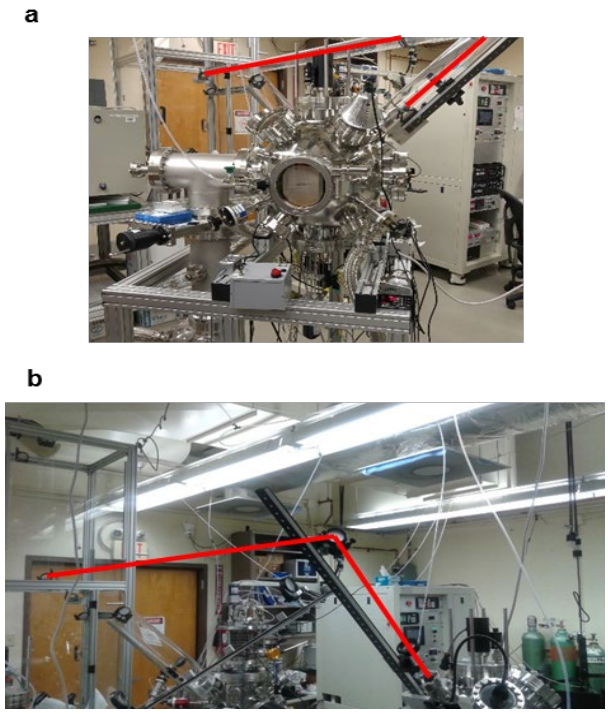

Figure B6 Past and current laser beam path for chamber 2. a, past laser beam path. The approximate beam path is indicated by the red line. Notice that the path is shielded. b, current unshielded beam path.

The clear plastic shielding is enough to stop the UV laser beam. The current location of chamber 2 is shown in Fig. B6b. At this time, the clear plastic shielding is still being designed and implemented. Note that the laser port is a reduced 4 ½ in. flange. The UV laser window is 2 ¾ in. where the laser enters the chamber (See Fig. B2a). Due to the lack of shielding, extra care is taken during thin film deposition to ensure that exposed skin is covered and that no one walks across the beam path when chamber 2 is in use.

REFERENCES

1 Cox, P. A. *Transition metal oxides: an introduction to their electronic structure and properties*. (Oxford University Press, 2010).

2 Zhang, L. *et al.* Correlated metals as transparent conductors. *Nature Materials* **15**, 204-210 (2016).

3 Ohtomo, A. & Hwang, H. Y. A high-mobility electron gas at the LaAlO3/SrTiO3 interface. *Nature* **427**, 423-425 (2004).

4 Kalabukhov, A. *et al.* Surface physics, nanoscale physics, low-dimensional systems-Effect of oxygen vacancies in the SrTiO3 substrate on the electrical properties of the LaAlO3/SrTiO3 interface. *Physical Review B* **75**, 121404R (2007).

5 Siemons, W. *et al.* Origin of Charge Density at LaAlO3 on SrTiO3 Heterointerfaces: Possibility of Intrinsic Doping. *Phys. Rev. Lett.* **98** (2007).

6 Herranz, G. *et al.* High mobility in LaAlO 3/SrTiO 3 heterostructures: Origin, dimensionality, and perspectives. *Physical Review Letters* **98**, 216803 (2007).

7 Reyren, N. *et al.* Superconducting interfaces between insulating oxides. *Science* **317**, 1196-1199 (2007).

8 Bert, J. A. *et al.* Direct imaging of the coexistence of ferromagnetism and superconductivity at the LaAlO3/SrTiO3 interface. *Nature Physics* **7**, 767 (2011).

9 Dikin, D. *et al.* Coexistence of Superconductivity and Ferromagnetism in Two Dimensions. *Physical Review Letters* **107** (2011).

10 Ohtomo, A., Muller, D., Grazul, J. & Hwang, H. Y. Artificial charge-modulationin atomic-scale perovskite titanate superlattices. *Nature* **419**, 378 (2002).

11 Biscaras, J. *et al.* Two-dimensional superconductivity at a Mott insulator/band insulator interface LaTiO3/SrTiO3. *Nature Communications* **1**, 89 (2010).

12 Seo, S. S. A. *et al.* Optical study of the free-carrier response of LaTiO3/SrTiO3 superlattices. *Physical Review Letters* **99**, 266801 (2007).

13 Kim, J. S. *et al.* Nonlinear Hall effect and multichannel conduction in LaTiO3/SrTiO3 superlattices. *Physical Review B* **82** (2010).

14 Choi, W. S. *et al.* Charge states and magnetic ordering in LaMnO3/SrTiO3 superlattices. *Physical Review B* **83**, 195113 (2011).

15 Chakhalian, J. *et al.* Orbital reconstruction and covalent bonding at an oxide interface. *Science* **318**, 1114-1117 (2007).

16 Gozar, A. *et al.* High-temperature interface superconductivity between metallic and insulating copper oxides. *Nature* **455**, 782-785 (2008).

17 Koida, T. *et al.* Effect of A-site cation ordering on the magnetoelectric properties in [(LaMnO3)m/(SrMnO3)m]n artificial superlattices. *Physical Review B* **66** (2002).

18 Hwang, H. Y. *et al.* Emergent phenomena at oxide interfaces. *Nature Materials* **11**, 103-113 (2012).

19 Baer, W. Free-Carrier Absorption in Reduced SrTiO3. *Physical Review* **144**, 734 (1966).
20 Lee, C., Destry, J. & Brebner, J. Optical absorption and transport in semiconducting SrTiO3. *Physical Review B* **11**, 2299 (1975).
21 Fujishima, Y., Tokura, Y., Arima, T. & Uchida, S. Optical-conductivity spectra of Sr(1-x)La(x)TiO3: Filling-dependent effect of the electron correlation. *Physical Review B* **46**, 11167-11170 (1992).
22 Ahrens, M., Merkle, R., Rahmati, B. & Maier, J. Effective masses of electrons in n-type SrTiO3 determined from low-temperature specific heat capacities. *Physica B: Condensed Matter* **393**, 239-248 (2007).
23 Connell, J. G. *et al.* Transparent conducting states induced by hydrogen-plasma *To be submitted to Nature Materials*.
24 Connell, J. G., Nichols, J., Gruenewald, J. H., Kim, D. W. & Seo, S. S. A. Conducting LaAlO3/SrTiO3 heterointerfaces on atomically-flat substrates prepared by deionized-water. *Scientific Reports* **6**, 23621 (2016).
25 Kittel, C. *Introduction to solid state physics*. (Wiley, 2005).
26 Weaver, H. E. Dielectric properties of single crystals of SrTiO3 at low temperatures. *Journal of Physics and Chemistry of Solids* **11**, 274-277 (1959).
27 Ziman, J. M. *Principles of the Theory of Solids*. (Cambridge University Press, 1972).
28 Siemons, W. *et al.* Dielectric-constant-enhanced Hall mobility in complex oxides. *Advanced Materials* **24**, 3965-3969 (2012).
29 Anderson, P. W. Absence of Diffusion in Certain Random Lattices. *Physical Review* **109**, 1492-1505 (1958).
30 Imada, M., Fujimori, A. & Tokura, Y. Metal-insulator transitions. *Reviews of Modern Physics* **70**, 1039-1263 (1998).
31 Efros, A. L. & Pollak, M. *Electron-electron interactions in disordered systems*. Vol. 10 (Elsevier, 1985).
32 Kim, K. W., Lee, J. S., Noh, T. W., Lee, S. R. & Char, K. Metal-insulator transition in a disordered and correlated SrTi1−xRuxO3 system: Changes in transport properties, optical spectra, and electronic structure. *Physical Review B* **71** (2005).
33 Fritsch, V. *et al.* Metal-to-insulator transition in La(1-x)Ba(x)TiO3. *Physical Review B* **64**, 045113 (2001).
34 Härdtl, K. H. & Wernicke, R. Lowering the Curie temperature in reduced BaTiO3. *Solid State Communications* **10**, 153-157 (1972).
35 Hwang, J., Kolodiazhnyi, T., Yang, J. & Couillard, M. Doping and temperature-dependent optical properties of oxygen-reduced BaTiO(3-d). *Physical Review B* **82**, 214109 (2010).
36 Jeong, I. K. *et al.* Structural evolution across the insulator-metal transition in oxygen-deficient BaTiO(3-d) studied using neutron total scattering and Rietveld analysis. *Physical Review B* **84**, 064125 (2011).
37 Kolodiazhnyi, T., Tachibana, M., Kawaji, H., Hwang, J. & Takayama-Muromachi, E. Persistence of Ferroelectricity in BaTiO3 through the Insulator-Metal Transition. *Physical Review Letters* **104**, 147602 (2010).

38 Arlt, G., Hennings, D. & de With, G. Dielectric properties of fine-grained barium titanate ceramics. *Journal of Applied Physics* **58**, 1619-1625 (1985).
39 Buchanan, R. C. & Park, T. *Materials Crystal Chemistry*. (CRC Press, 1997).
40 Liang, X., Meng, Z. & Wu, W. Effect of acceptor and donor dopants on the dielectric and tunable properties of barium strontium titanate. *Journal of the American Ceramic Society* **87**, 2218-2222 (2004).
41 Waser, R. Solubility of Hydrogen Defects in Doped and Undoped BaTiO3. *Journal of the American Ceramic Society* **71**, 58-63 (1988).
42 Hosono, H., Kageyama, H., Kobayashi, Y., Takano, M. & Yajima, T. Perovskite oxide containing hydride ion, and method for manufacturing same. United States patent US20140128252 A1 (2014).
43 Sakaguchi, T. *et al.* Oxyhydrides of (Ca,Sr,Ba)TiO3 Perovskite Solid Solutions. *Inorganic Chemistry* **51**, 11371-11376 (2012).
44 Yajima, T. *et al.* Epitaxial Thin Films of ATiO3–xHx (A = Ba, Sr, Ca) with Metallic Conductivity. *Journal of the American Chemical Society* **134**, 8782-8785 (2012).
45 Bouilly, G. *et al.* Electrical Properties of Epitaxial Thin Films of Oxyhydrides ATiO(3–x)H(x) (A = Ba and Sr). *Chemistry of Materials* **27**, 6354-6359 (2015).
46 Chen, X., Liu, L., Yu, P. Y. & Mao, S. S. Increasing Solar Absorption for Photocatalysis with Black Hydrogenated Titanium Dioxide Nanocrystals. *Science* **331**, 746-750 (2011).
47 Yoon, H. *et al.* Reversible phase modulation and hydrogen storage in multivalent VO2 epitaxial thin films. *Nature Materials* **15**, 1113-1119 (2016).
48 Lu, N. *et al.* Electric-field control of tri-state phase transformation with a selective dual-ion switch. *Nature* **546**, 124 (2017).
49 Wang, M. *et al.* Electric-Field-Controlled Phase Transformation in WO3 Thin Films through Hydrogen Evolution. *Advanced Materials* **29**, 1703628 (2017).
50 Li, Z. *et al.* Electric-field Control of Magnetism with Emergent Topological Hall Effect in SrRuO3 through Proton Evolution. *arXiv preprint arXiv:1811.10794* (2018).
51 Morito, K. & Sasajima, Y. Influence of Hydrogen on Electrical Properties of Pt/(Ba,Sr)TiO3/Pt Thin Film Capacitors. *Integrated Ferroelectrics* **86**, 3-12 (2007).
52 Islam, S. Z. *et al.* Hydrogen incorporation by plasma treatment gives mesoporous black TiO2 thin films with visible photoelectrochemical water oxidation activity. *Microporous and Mesoporous Materials* **261**, 35-43 (2018).
53 Liedtke, R., Grossmann, M. & Waser, R. Capacitance and admittance spectroscopy analysis of hydrogen-degraded Pt/(Ba,Sr)TiO3/Pt thin-film capacitors. *Applied Physics Letters* **77**, 2045-2047 (2000).
54 Hadad, D. *et al.* The effects of forming gas anneal on the electrical characteristics of Ir-electroded BST thin film capacitors. *Integrated Ferroelectrics* **17**, 461-469 (2006).
55 Morito, K. *et al.* Influence of Hydrogen Atoms on Electrical Properties of BST Thin Film Capacitors. *Key Engineering Materials* **388**, 167-170 (2009).

56 Liang, Y.-C. Hydrogen-induced degradation in physical properties of dielectric-enhanced Ba0.6Sr0.4TiO3/SrTiO3 artificial superlattices. *Electrochemical and Solid-State Letters* **13**, G91-G94 (2010).
57 Hayashi, K., Matsuishi, S., Kamiya, T., Hirano, M. & Hosono, H. Light-induced conversion of an insulating refractory oxide into a persistent electronic conductor. *Nature* **419**, 462 (2002).
58 Yeow, Y. T., Lamb, D. R. & Brotherton, S. D. An investigation of the influence of low-temperature annealing treatments on the interface state density at the Si-SiO2. *Journal of Physics D: Applied Physics* **8**, 1495-1506 (1975).
59 Do Thanh, L. & Balk, P. Elimination and Generation of Si - SiO2 Interface Traps by Low Temperature Hydrogen Annealing. *Journal of The Electrochemical Society* **135**, 1797-1801 (1988).
60 Syamaprasad, U., Galgali, R. & Mohanty, B. Dielectric properties of the Ba1−xSrxTiO3 system. *Materials Letters* **7**, 197-200 (1988).
61 Nakamura, T., Yamanaka, Y., Morimoto, A. & Shimizu, T. Effect of Oxygen Pressure on (BaxSr1-x)TiO3 Thin Films by Pulsed Laser Ablation. *Japanese Journal of Applied Physics* **34**, 5150-5153 (1995).
62 Wang, S. Y. *et al.* Dielectric and Ferroelectric Properties of Ba1-xSrxTiO3 Thin Films Prepared by Pulsed Laser Deposition. *Key Engineering Materials* **280-283**, 81-84 (2004).
63 Kawasaki, M. *et al.* Atomic control of the SrTiO3 crystal surface. *Science* **266**, 1540-1542 (1994).
64 Hatch, R. C. *et al.* Surface electronic structure for various surface preparations of Nb-doped SrTiO3 (001). *Journal of Applied Physics* **114**, 103710 (2013).
65 Chambers, S. A., Droubay, T. C., Capan, C. & Sun, G. Y. Unintentional F doping of SrTiO3(001) etched in HF acid-structure and electronic properties. *Surface Science* **606**, 554-558 (2012).
66 Ohsawa, T., Shimizu, R., Iwaya, K., Shiraki, S. & Hitosugi, T. Negligible Sr segregation on SrTiO3(001)-(13×13)-R33.7° reconstructed surfaces. *Applied Physics Letters* **108**, 161603 (2016).
67 Hatch, R. C., Choi, M., Posadas, A. B. & Demkov, A. A. Comparison of acid- and non-acid-based surface preparations of Nb-doped SrTiO3 (001). *Journal of Vacuum Science & Technology B* **33**, 061204 (2015).
68 Connell, J. G., Isaac, B. J., Ekanayake, G. B., Strachan, D. R. & Seo, S. S. A. Preparation of atomically flat SrTiO3 surfaces using a deionized-water leaching and thermal annealing procedure. *Applied Physics Letters* **101**, 251607 (2012).
69 Ginley, D. S. & Perkins, J. D. *Handbook of transparent conductors*. (Springer, 2011).
70 Thompson, J. *et al.* Alleviating polarity-conflict at the heterointerfaces of KTaO3/GdScO3 polar complex-oxides. *Applied Physics Letters* **105**, 102901 (2014).
71 Tadatsugu, M. Transparent conducting oxide semiconductors for transparent electrodes. *Semiconductor Science and Technology* **20**, S35 (2005).
72 Ellmer, K. Past achievements and future challenges in the development of optically transparent electrodes. *Nature Photonics* **6**, 809-817 (2012).

73 Freeman, A. J., Poeppelmeier, K. R., Mason, T. O., Chang, R. P. H. & Marks, T. J. Chemical and Thin-Film Strategies for New Transparent Conducting Oxides. *MRS Bulletin* **25**, 45-51 (2011).
74 Du, H., Fisher, P. J., Skowronski, M., Salvador, P. A. & Maksimov, O. Growth and structural characterization of epitaxial Ba0.6Sr0.4TiO3 films deposited on REScO3 (110) (RE= Dy, Gd) substrates using pulsed laser deposition. *Journal of Crystal Growth* **310**, 1991-1998 (2008).
75 Gayathri, N., Raychaudhuri, A., Xu, X., Peng, J. & Greene, R. Electronic conduction in LaNiO3-d: the dependence on the oxygen stoichiometry. *Journal of Physics: Condensed Matter* **10**, 1323 (1998).
76 Gruenewald, J. H. *et al.* Compressive strain-induced metal–insulator transition in orthorhombic SrIrO3 thin films. *Journal of Materials Research* **29**, 2491-2496 (2014).
77 Naldoni, A. *et al.* Effect of Nature and Location of Defects on Bandgap Narrowing in Black TiO2 Nanoparticles. *Journal of the American Chemical Society* **134**, 7600-7603 (2012).
78 Selcuk, S., Zhao, X. & Selloni, A. Structural evolution of titanium dioxide during reduction in high-pressure hydrogen. *Nature Materials* **17**, 923-928 (2018).
79 Mott, N. F. Conduction in non-crystalline materials. *Philosophical Magazine* **19** (1969).
80 Mott, N. F. Conduction in glasses containing transition metal ions. *Journal of Non-Crystalline Solids* **1**, 1-17 (1968).
81 Mott, N. *Metal-insulator transitions*. (CRC Press, 1990).
82 Bergmann, G. Weak localization in thin films: a time-of-flight experiment with conduction electrons. *Physics Reports* **107**, 1-58 (1984).
83 Rosenbaum, T. *et al.* Low-temperature magnetoresistance of a disordered metal. *Physical Review Letters* **47**, 1758-1761 (1981).
84 Dugdale, J. S. *The electrical properties of disordered metals*. (Cambridge University Press, 2005).
85 Haacke, G. New figure of merit for transparent conductors. *Journal of Applied Physics* **47**, 4086-4089 (1976).
86 Frederikse, H. P. R. & Candela, G. A. Magnetic Susceptibility of Insulating and Semiconducting Strontium Titanate. *Physical Review* **147**, 583-584 (1966).
87 Kim, J. *et al.* Surface chemistry modification in ITO films induced by Sn2+ ionic state variation. *Current Applied Physics* **17**, 1415-1421 (2017).
88 Moulder, J. F. & Chastain, J. *Handbook of X-ray Photoelectron Spectroscopy: A Reference Book of Standard Spectra for Identification and Interpretation of XPS Data*. (Physical Electronics Division, Perkin-Elmer Corporation, 1992).
89 Miot, C., Husson, E., Proust, C., Erre, R. & Coutures, J. Residual carbon evolution in BaTiO3 ceramics studied by XPS after ion etching. *Journal of the European Ceramic Society* **18**, 339-343 (1998).
90 Hossain, J. *et al.* Barium hydroxide hole blocking layer for front-and back-organic/crystalline Si heterojunction solar cells. *Journal of Applied Physics* **122**, 055101 (2017).

91 Bender, H., Chen, W., Portillo, J., Van den Hove, L. & Vandervorst, W. AES and XPS analysis of the interaction of Ti with Si and SiO2 during RTA. *Applied Surface Science* **38**, 37-47 (1989).
92 Gonbeau, D. *et al.* XPS study of thin films of titanium oxysulfides. *Surface Science* **254**, 81-89 (1991).
93 Vasquez, R. P. X-ray photoelectron spectroscopy study of Sr and Ba compounds. *Journal of Electron Spectroscopy and Related Phenomena* **56**, 217-240 (1991).
94 Wang, L. *et al.* Hole-induced electronic and optical transitions in La1-xSrxFeO3 epitaxial thin films. *Physical Review Materials* **3**, 025401 (2019).
95 Fan, J. C. C. & Goodenough, J. B. X-ray photoemission spectroscopy studies of Sn-doped indium-oxide films. *Journal of Applied Physics* **48**, 3524-3531 (1977).
96 Xu, M. *et al.* A green heterogeneous synthesis of N-doped carbon dots and their photoluminescence applications in solid and aqueous states. *Nanoscale* **6**, 10307-10315 (2014).
97 Ulaganathan, M. *et al.* Recent Advancements in All-Vanadium Redox Flow Batteries. *Advanced Materials Interfaces* **3**, 1500309 (2016).
98 Sun, T. & Lu, M. Band-structure modulation of SrTiO3 by hydrogenation for enhanced photoactivity. *Applied Physics A* **108**, 171-175 (2012).
99 Brillson, L. J. *Surfaces and Interfaces of Electronic Materials*. (Wiley, 2012).
100 Koster, G., Kropman, B. L., Rijnders, G. J., Blank, D. H. & Rogalla, H. Quasi-ideal strontium titanate crystal surfaces through formation of strontium hydroxide. *Applied Physics Letters* **73**, 2920-2922 (1998).
101 Lide, D. R. *CRC Handbook of Chemistry and Physics*. 85th edn, (CRC Press, 2004).
102 Seo, S. S. A. *et al.* Multiple conducting carriers generated in LaAlO3/SrTiO3 heterostructures. *Applied Physics Letters* **95**, 082107 (2009).
103 Shalom, M. B., Ron, A., Palevski, A. & Dagan, Y. Shubnikov–de Haas oscillations in SrTiO3/LaAlO3 interface. *Physical Review Letters* **105**, 206401 (2010).
104 Lerer, S., Shalom, M. B., Deutscher, G. & Dagan, Y. Low-temperature dependence of the thermomagnetic transport properties of the SrTiO3/LaAlO3 interface. *Physical Review B* **84**, 075423 (2011).
105 Fête, A. *et al.* Growth-induced electron mobility enhancement at the LaAlO3/SrTiO3 interface. *Applied Physics Letters* **106**, 051604 (2015).
106 Xie, Y., Bell, C., Hikita, Y., Harashima, S. & Hwang, H. Y. Enhancing electron mobility at the LaAlO3/SrTiO3 interface by surface control. *Advanced Materials* **25**, 4735-4738 (2013).
107 Kim, H. *et al.* Influence of gas ambient on charge writing at the LaAlO3/SrTiO3 heterointerface. *ACS Applied Materials & Interfaces* **6**, 14037-14042 (2014).
108 Kim, S. K. *et al.* Electric-field-induced Shift in the Threshold Voltage in LaAlO3/SrTiO3 Heterostructures. *Scientific Reports* **5**, 8023 (2015).
109 Kareev, M. *et al.* Atomic control and characterization of surface defect states of TiO2 terminated SrTiO3 single crystals. *Applied Physics Letters* **93**, 061909 (2008).
110 Biswas, A. *et al.* Universal Ti-rich termination of atomically flat SrTiO3 (001), (110), and (111) surfaces. *Applied Physics Letters* **98**, 051904 (2011).

111 Ohnishi, T. *et al.* Preparation of thermally stable TiO2-terminated SrTiO3 (100) substrate surfaces. *Applied Physics Letters* **85**, 272, doi:10.1063/1.1771461 (2004).
112 Tench, D. & Raleigh, D. Electrochemical Processes on Strontium Titanate Electrodes. *National Bureau Standards Special Publications* **455**, 229-240 (1976).
113 Karthäuser, S., Speier, W., & Szot, K. Verfahren zur Herstellung einer B-terminierten Oberfläche auf Perowskit-Einkristallen. Germany patent (2005).
114 Boschker, J. & Tybell, T. Qualitative determination of surface roughness by in situ reflection high energy electron diffraction. *Applied Physics Letters* **100**, 151604 (2012).
115 Bell, C., Harashima, S., Hikita, Y. & Hwang, H. Thickness dependence of the mobility at the LaAlO3/SrTiO3 interface. *Applied Physics Letters* **94**, 222111 (2009).
116 Rotella, H. *et al.* Two components for one resistivity in LaVO3/SrTiO3 heterostructure. *Journal of Physics: Condensed Matter* **27**, 095603 (2015).
117 Arushanov, E. & Chuiko, G. The magnetic field dependence of kinetic coefficients of cadmium arsenide single crystals. *Physica Status Solidi (a)* **17**, K135-K138 (1973).
118 Laiho, R. *et al.* Hall effect and band structure of p-CdSb in strong magnetic field. *Semiconductor Science and Technology* **19**, 602 (2004).
119 Chen, Y. *et al.* Metallic and Insulating Interfaces of Amorphous SrTiO3-Based Oxide Heterostructures. *Nano Letters* **11**, 3774-3778 (2011).
120 Hotta, Y., Susaki, T. & Hwang, H. Polar Discontinuity Doping of the LaVO3/SrTiO3 Interface. *Physical Review Letters* **99** (2007).
121 Moetakef, P. *et al.* Electrostatic carrier doping of GdTiO3/SrTiO3 interfaces. *Applied Physics Letters* **99**, 232116 (2011).
122 Annadi, A. *et al.* Electronic correlation and strain effects at the interfaces between polar and nonpolar complex oxides. *Physical Review B* **86**, 085450 (2012).
123 Gunkel, F. *et al.* Stoichiometry dependence and thermal stability of conducting NdGaO3/SrTiO3 heterointerfaces. *Applied Physics Letters* **102**, 071601 (2013).
124 Verma, A., Raghavan, S., Stemmer, S. & Jena, D. Ferroelectric transition in compressively strained SrTiO3 thin films. *Applied Physics Letters* **107**, 192908 (2015).
125 Choquette, A. K. *et al.* Synthesis, Structure, and Spectroscopy of Epitaxial EuFeO3 Thin Films. *Crystal growth & design* **15**, 1105-1111 (2015).
126 Gallagher, P. *et al.* A high-mobility electronic system at an electrolyte-gated oxide surface. *Nature Communications* **6**, 6437 (2015).
127 KC, A., Borisov, P., Shvartsman, V. V. & Lederman, D. Weak ferromagnetism and short range polar order in NaMnF3 thin films. *Applied Physics Letters* **110**, 092901 (2017).
128 Biswas, A., Yang, C.-H., Ramesh, R. & Jeong, Y. H. Atomically flat single terminated oxide substrate surfaces. *Progress in Surface Science* **92**, 117-141 (2017).
129 Gellé, F. *et al.* Guideline to atomically flat TiO2-terminated SrTiO3(001) surfaces. *Surface Science* **677**, 39-45 (2018).

130 Brinkman, A. *et al.* Magnetic effects at the interface between non-magnetic oxides. *Nature Materials* **6**, 493-496 (2007).
131 Yamada, H., Xiang, P. H. & Sawa, A. Phase evolution and critical behavior in strain-tuned LaMnO3-SrMnO3 superlattices. *Physical Review B* **81** (2010).
132 Szot, K. & Speier, W. Surfaces of reduced and oxidized SrTiO3 from atomic force microscopy. *Physical Review B* **60**, 5909-5926 (1999).
133 Ngai, J. H. *et al.* Achieving A-site termination on La(0.18)Sr(0.82)Al(0.59)Ta(0.41)O(3) substrates. *Advanced Materials* **22**, 2945-2948 (2010).
134 Adair, J. H., Crampo, J., Mandanas, M. M. & Suvaci, E. The Role of Material Chemistry in Processing BaTiO3 in Aqueous Suspensions. *Journal of the American Ceramic Society* **89**, 1853-1860 (2006).
135 Vance, E. R., Angel, P. J., Begg, B. D. & Day, R. A. Zirconolite-Rich Titanate Ceramics for High-Level Actinide Wastes. *MRS Online Proceedings Library* **333**, 293 (1993).
136 Chang, J., Park, Y. S. & Kim, S. K. Atomically flat single-terminated SrTiO3 (111) surface. *Applied Physics Letters* **92**, 152910 (2008).
137 Gruenewald, J. H., Nichols, J. & Seo, S. S. A. Pulsed laser deposition with simultaneous in situ real-time monitoring of optical spectroscopic ellipsometry and reflection high-energy electron diffraction. *Review of Scientific Instruments* **84**, 043902 (2013).
138 Souri, M. *Electronic and optical properties of metastable epitaxial thin films of layered iridates* Theses and Dissertations-Physics and Astronomy, 60, University of Kentucky, (2018).

VITA

John Gerard Connell

EDUCATION

University of Kentucky, Lexington, Kentucky

Ph. D. in Condensed Matter Physics, 2019 (expected)

University of Kentucky, Lexington, Kentucky

M. S. in Physics (2013)

University of Scranton, Scranton, Pennsylvania

B.S. in Physics (2009)

PUBLICATIONS

1. *Transparent Conducting Titanates induced by hydrogen-plasma* **J. G. Connell**, N. Wanninayake, M. Souri, J. Kim, J. Johnson, J. W. Brill, J. Hwang, D. Y. Kim, and A. Seo (To be submitted to Nature Materials)
2. *Electronic and optical properties of La-doped $Sr_3Ir_2O_7$ epitaxial thin films* M. Souri, J. Terzic, J. M. Johnson, **J. G. Connell**, J. H. Gruenewald, J. Thompson, J. W. Brill, J. Hwang, G. Cao, and A. Seo Phys. Rev. Materials **2**, 024803 (2018).
3. *Optical signatures of spin-orbit exciton in bandwidth controlled Sr_2IrO_4 epitaxial films via high-concentration Ca and Ba doping* M. Souri, B. H. Kim, J. H. Gruenewald, **J. G. Connell**, J. Thompson, J. Nichols, J. Terzic, B. I. Min, J. W. Brill, G. Cao, and A. Seo, Phys. Rev. B **95**, 235125 (2017).
4. *Selective growth of epitaxial Sr_2IrO_4 by controlling plume dimensions in pulsed laser deposition* S. S. A. Seo, J. Nichols, J. Hwang, J. Terzic, J. H. Gruenewald, M. Souri, J. Thompson, **J. G. Connell**, and G. Cao Appl. Phys. Lett. **109**, 201901 (2016).
5. *Enhanced metallic properties of $SrRuO_3$ thin film electrodes via kinetically controlled laser ablation* J. Thompson, J. Nichols, S. Lee, S. Ryee, J. H. Gruenewald, **J. G. Connell**, J. M. Johnson, J. Hwang, M. J. Han, H. N. Lee, D.-W. Kim, and S. S. A. Seo Appl. Phys. Lett. **109**, 161902 (2016).
6. *Conducting $LaAlO_3/SrTiO_3$ heterointerfaces on atomically flat substrates prepared by deionized-water* **J. G. Connell**, J. Nichols, J. H. Gruenewald, D.-W. Kim, and S. S. A. Seo Sci. Rep. **6**, 23621 (2016).

7. *Domain wall conductivity in semiconducting hexagonal ferroelectric $TbMnO_3$ thin films* D. J. Kim, **J. G. Connell**, S. S. A. Seo, and A. Gruverman Nanotechnology **27**, 155705 (2016).
8. *Room-temperature ferroelectricity in hexagonal $TbMnO_3$ thin films* D. J. Kim, T. R. Paudel, H. Lu, J. D. Burton, **J. G. Connell**, E. Y. Tsymbal, S. S. A. Seo, and A. Gruverman Adv. Mater. **26**, 7660 (2014).
9. *Alleviating polarity-conflict at the heterointerfaces of $KTaO_3/GdScO_3$ polar complex-oxides* J. Thompson, J. Hwang, J. Nichols, **J. G. Connell**, S. Stemmer, and S. S. A. Seo Appl. Phys. Lett. **105**, 102901 (2014).
10. *Preparation of atomically-flat $SrTiO_3$ surfaces using a deionized-water leaching and thermal annealing procedure* **J. G. Connell**, B. J. Isaac, G. B. Ekanayake, D. R. Strachan, and S. S. A. Seo Appl. Phys. Lett. **101**, 251607 (2012).